# Extinction-to-backscatter Ratios of Saharan Dust Layers Derived from In-Situ Measurements and CALIPSO Overflights during NAMMA

A. H. Omar, Z. Liu, M. Vaughan, K. L. Thornhill, C. Kittaka, S. Ismail, Y. Hu, G. Chen, K. Powell, D. Winker, C. Trepte, E. L. Winstead, B. E Anderson

## Abstract

We determine the extinction-to-backscatter ($S_a$) ratios of dust using (1) airborne in-situ measurements of microphysical properties, (2) modeling studies, and (3) the Cloud-Aerosol Lidar and Infrared Pathfinder Satellite Observations (CALIPSO) observations recorded during the NASA African Monsoon Multidisciplinary Analyses (NAMMA) field experiment conducted from Sal, Cape Verde during Aug-Sept 2006. Using CALIPSO measurements of the attenuated backscatter of lofted Saharan dust layers, we apply the transmittance technique to estimate dust $S_a$ ratios at 532 nm and a 2-color method to determine the corresponding 1064 nm $S_a$. This method yielded dust $S_a$ ratios of 39.8 ± 1.4 sr and 51.8 ± 3.6 sr at 532 nm and 1064 nm, respectively. Secondly, $S_a$ at both wavelengths is independently calculated using size distributions measured aboard the NASA DC-8 and estimates of Saharan dust complex refractive indices applied in a T-Matrix scheme. We found $S_a$ ratios of 39.1 ± 3.5 sr and 50.0 ± 4 sr at 532 nm and 1064 nm, respectively, using the T-Matrix calculations applied to measured size spectra. Finally, in situ measurements of the total scattering (550 nm) and absorption coefficients (532 nm) are used to generate an extinction profile that is used to constrain the CALIPSO 532 nm extinction profile and thus generate a stratified 532 nm $S_a$. This method yielded an $S_a$ ratio at 532 nm of 35.7 sr in the dust layer and 25 sr in the marine boundary layer consistent with a predominantly seasalt aerosol near the ocean surface. Combinatorial simulations using noisy size spectra and refractive indices were used to estimate the mean and uncertainty (one standard deviation) of these $S_a$ ratios. These simulations produced a mean (± uncertainty) of 39.4 (± 5.9) sr and 56.5 (± 16.5) sr at 532 nm and 1064 nm, respectively, corresponding to percent uncertainties of 15% and 29%. These results will provide a measurements-based estimate of the dust $S_a$ for use in backscatter lidar inversion algorithms such as CALIOP.

## 1. Introduction

Lidar is a powerful tool for studying the vertical distribution of aerosols and clouds in the atmosphere. Of particular importance is the distribution and transport of Saharan dust systems. The deployment of CALIPSO (Cloud-Aerosol Lidar and Infrared Pathfinder Satellite Observations), a joint NASA-CNES satellite mission, has enabled vertically resolved measurements of Sahara air layer(s) (SAL) which will provide significant insights into properties of Sahara dust aerosols. CALIPSO is designed to provide measurements to advance our understanding of the role of aerosols and clouds in the climate system [*Winker et al.*, 2009]. The Cloud-Aerosol LIdar with Orthogonal Polarization [CALIOP, *Winker et al.*, 2007] is the primary instrument on the CALIPSO satellite. CALIOP is designed to acquire vertical profiles of elastic backscatter at two wavelengths (1064 nm and 532 nm) from a near nadir-viewing geometry during both day and night phases of the orbit. In addition to the total backscatter at the two wavelengths, CALIOP also provides profiles of linear depolarization at 532 nm. Accurate aerosol and cloud heights and retrievals of extinction coefficient profiles are derived from the total backscatter measurements [*Vaughan et al.*, 2009] The depolarization measurements enable the discrimination between ice clouds and water clouds [*Hu et al.*, 2009] and the identification of non-spherical aerosol particles [*Liu et al.*, 2009]. Additional information, such as estimates of particle size for the purpose of discriminating between clouds and aerosols, are obtained from the ratios of the signals obtained at the two wavelengths. On April 28, 2006, the CALIPSO satellite was launched into a low earth sun-synchronous orbit at a 705-km altitude, and an inclination of 98.2 degrees. A few months later, in August 2006, the NASA African Monsoon Multidisciplinary Analyses (NAMMA)

54 campaign commenced at the Cape Verde Islands, 350 miles off the coast of Senegal in
55 West Africa. NAMMA was designed to study the evolution of precipitating convective
56 systems, largely as this evolution pertained to the SAL and its role in the tropical
57 cyclogenesis. Several aircraft flights were dedicated to nearly coincident measurements
58 with NASA's orbiting satellites (including Aqua, TRMM, and CloudSat/CALIPSO). For
59 this study, we use data collected aboard NASA's DC-8 medium altitude research aircraft
60 outfitted with, among other instruments, a full suite of sensors and probes designed to
61 measure aerosol microphysical and optical properties. Relevant parameters include high
62 spatial-resolution scattering and absorption coefficients at multiple wavelengths in the
63 visible spectrum and dry particle size distributions over the 0.08 to 10 μm diameter range
64 [*Chen et al.*, 2010].
65 Depending on the mineralogical composition, the SAL can have a significant impact on
66 both the radiation balance and cloud processes. Dust particles scatter in the shortwave
67 regime (cooling the planet) and absorb both shortwave and longwave radiation (heating
68 the planet). By some estimates the anthropogenic forcing due to dust is comparable to the
69 forcing by all other anthropogenic aerosols combined [*Sokolik and Toon*, 1996]. Saharan
70 dust influences cyclone activity and convection in the region off the west coast of Africa
71 and air quality as far west as the US east coast and Gulf of Mexico. There have been
72 reports of causal links between cyclone activity and dust loading suggesting that perhaps
73 the Sahara dust layer acts to inhibit cyclone development [*Dunion and Velden*, 2004] and
74 more generally convection [*Wong and Dessler*, 2005]. Sahara dust is unique in its ability
75 to maintain layer integrity as it is transported over long distances (~7500 km) to the
76 Americas [*Liu et al.*, 2008; *Maring et al.*, 2003; *Savoie and Prospero*, 1976]. The

77 presence of Sahara dust layers have been found to perturb ice nuclei (IN) concentrations
78 as far away as in Florida. During CRYSTAL-FACE (Cirrus Regional Study of Tropical
79 Anvils and Cirrus Layers - Florida Area Cirrus Experiment), DeMott et al. [2003] found
80 that IN concentrations were significantly enhanced in heterogeneous ice nucleation
81 regimes warmer than -38°C, when Saharan dust layers are present. It is therefore
82 important to study the distribution and optical properties of Sahara dust.
83 In order to estimate the optical depth of the Sahara dust layers from elastic backscatter
84 lidar measurements, the $S_a$ ratio must be known or prescribed. Given aerosol free regions
85 above and below a lofted dust aerosol layer, $S_a$ can be calculated from the attenuated
86 backscatter profile of a space-based lidar return [*Young*, 1995]. $S_a$ for dust aerosols is
87 dependent on the mineral composition, size distribution, and shape parameters (e.g.,
88 aspect ratio, and complexity factor). All of these are highly variable and for the most part
89 not well known. For these reasons, $S_a$ obtained from scattering models have larger
90 uncertainties than models of the nearly spherical urban pollution or marine aerosols.
91 There have been several studies and measurements of dust $S_a$ at 532 nm [*Ackermann*,
92 1998; *Anderson et al.*, 2000; *Berthier et al.*, 2006; *Di Iorio et al.*, 2003; *Di Iorio et al.*,
93 2009; *Muller et al.*, 2007; *Müller et al.*, 2000; *Tesche et al.*, 2009] and relatively few such
94 measurements or studies of dust $S_a$ at 1064 nm [*Ackermann*, 1998; *Liu et al.*, 2008;
95 *Tesche et al.*, 2009]. Prior to NAMMA, there were a number of vertically-resolved
96 measurements of Saharan dust microphysical and optical properties including AMMA
97 and DODO campaigns  NAMMA studies along with CALIPSO measurements provide a
98 unique opportunity to compare extinction measurements derived from in situ profile
99 measurements of total scattering and absorption aboard the NASA DC-8 and CALIPSO

extinction profiles estimated from two wavelength retrieval methods. These profiles by extension provide the constraints from which the lidar ratios can be determined as explained in the following sections. Section 2 discusses the CALIPSO lidar data and its analysis. The NAMMA data and analyses are discussed in Section 3, and coincident CALIPSO-NAMMA measurements are presented in Section 4. In Section 5, the size distributions measured during NAMMA aboard the DC-8 are implemented in a T-Matrix scheme to estimate profiles of $S_a$ ratios. Section 6 discusses the uncertainty in $S_a$ using a combinatorial method.

## 2. CALIPSO Lidar Data and Extinction-to-Backscatter Ratio Retrieval Methods

The CALIPSO lidar data used for these studies are the version 2.01 lidar level 1 attenuated backscatter returns at the 532 nm perpendicular and parallel channels, and 1064 nm total attenuated backscatter. The volume depolarization ratio is determined from the perpendicular and parallel channels and used to identify dust aerosols [*Liu et al.*, 2009; *Omar et al.*, 2009]. For NAMMA underflights of CALIPSO and near spatial coincidences where both missions observed dust layers of optical depths greater than about 0.3, we compare the extinction profiles from in situ measurements to CALIPSO profiles. In such cases, we calculate the extinction using $S_a$ that was determined using the transmittance method or an $S_a$ ratio constrained by the in-situ extinction profiles. In both cases, we use the 2-color methods to retrieve the 1064-nm $S_a$, after determining the 532-nm $S_a$. These two methods, transmittance and 2-color, are discussed below.

### 2.1. Transmittance Methods

The transmittance method uses the following equation describing the relationship between optical depth and integrated attenuated backscatter, as in Platt [1973]:

$$\gamma' = \frac{1}{2\eta S_a}\left(1 - \exp\left(-2\eta\tau\right)\right) \quad (1)$$

Here $\gamma'$ is the integrated (from layer base to top) attenuated backscatter,

$$\gamma' = \int_{base}^{top} \beta_a(r) T_a^{\,2}(r) dr \quad (2)$$

$\tau$ is optical depth, $\eta$ is a multiple scattering parameter, $T^2 = \exp(-2\eta\tau)$ is the layer-effective two-way transmittance, and $S_a = \sigma_a/\beta_a$ where $\beta_a$ is the aerosol backscatter coefficient and $\sigma_a$ is the aerosol extinction coefficient. This ratio is assumed constant throughout a feature. Note that the quantities $S_a$, $\gamma'$, and $\tau$ describe characteristics of an aerosol layer, i.e., they are associated with the backscatter and extinction of aerosol particles only. If we define an effective $S_a$ ratio, $S^* = \eta S_a$, we can rewrite Eq. (1) as follows:

$$S^* = \frac{1 - T^2}{2\gamma'} \quad (3)$$

The effective two-way transmittance is typically obtained by fitting the returns both above and below a feature to a reference clear air scattering profile obtained from local

143 rawinsonde measurements or meteorological model data [*Young*, 1995]. In this study, the
144 transmittance method is used to determine S* from the 532-nm CALIPSO measurements
145 whenever clear air scattering signals are available both above and below an aerosol layer.
146 However, the same method is not applicable to the 1064-nm CALIPSO measurements,
147 because a reliable measurement of the clear air scattering at 1064 nm, which is about 16
148 times smaller than that at 532 nm, is not available. To determine S* at 1064 nm, the 2-
149 color method described in the next subsection is used.
150

151 **2.2. The 2-Color Method**

152 The 2-color or two-wavelength method was first proposed by Sasano and Browell
153 [*Sasano and Browell*, 1989] and adapted to space-borne lidar measurements using an
154 optimization technique by Vaughan et al. [2004]. The method requires *apriori* knowledge
155 of $S_a$ at 532 nm and a suitable profile of 532-nm attenuated backscatter amenable to the
156 calculation of 532-nm aerosol backscatter coefficient profiles. For the NAMMA cases
157 described below these preconditions were satisfied. Whenever a suitable region of clear
158 air was identified both above and below an aerosol layer, the $S_a$ at 532 nm was
159 determined using the transmittance method described above. Here clear air layer is
160 defined as a region of low attenuated scattering ratios with a mean value equal to or less
161 than 1 and a slope with respect to altitude of approximately zero. This is further
162 confirmed by low volume depolarization ratios in a small region (~ 1/2 km) below the
163 aerosol layer. In cases where coincident NAMMA measurements are available, $S_a$ ratio at
164 532 nm is the value that provides the best fit between the retrieved CALIPSO extinction
165 profiles and the NAMMA in situ extinction profiles obtained by summing the total

166 scattering and absorption measured by a nephelometer and a Particle Soot/Absorption
167 Photometer (PSAP), respectively, aboard the DC-8.
168
169 Once $S_a$ ratio is determined at 532 nm, the value at 1064 nm can be calculated using the
170 2-color method. We note that this technique can be used to derive $S_a$ at 532 nm if the
171 value at 1064 nm is known. Given a solution of the particulate backscatter at 532 nm,
172 $\beta_{532,p}$, the 2-color method uses a least squares method to minimize the difference between
173 the measured attenuated total backscatter at 1064 nm, $B_{1064}$, and the attenuated
174 backscatter at 1064 nm (right hand side of eq. (4)) reconstructed from the extinction and
175 backscatter coefficients at 532 nm.
176

177
$$\begin{aligned} B_{1064}(r) &= \left(\beta_{m,1064}(r) + \beta_{p,1064}\right) \cdot T^2_{p,1064}(r) \\ &= \left(\beta_{m,1064}(r) + \underline{\chi} \cdot \beta_{p,532}(r)\right) \cdot \exp\left(-2 \cdot \underline{S_{1064}} \cdot \underline{\chi} \cdot \gamma_{532}(r)\right) \end{aligned} \quad (4)$$

178
179 The only unknowns (underlined) in eq.(4), are the $S_a$ ratio at 1064 nm, $S_{1064}$, and the
180 backscatter color ratio, $\chi$ (defined as $\beta_{1064,p}/\beta_{532,p}$). These are both intensive aerosol
181 properties defined by the layer composition, size distribution, and shape of its constituent
182 particles. Since these characteristics do not vary substantially in a given aerosol layer, we
183 make the assumption that $S_{1064}$ and $\chi$ are constant within the layer. The algorithm details
184 and optimization techniques are discussed at length in Vaughan (2004) and Vaughan et
185 al. [2004]

## 3. Numerical Calculation Based on NAMMA In-situ Measurements

### 3.1. Aerosol Microphysical Properties

We use measurements of the aerosol size distributions based on number from the Aerodynamic Particle Sizer (APS, TSI Incorporated, Shoreview, MN) and the Ultra-High Sensitivity Aerosol Spectrometer (UHSAS, Droplet Measuring Systems, Boulder, CO). The UHSAS measures the fine mode aerosol size distributions from 0.06 to 0.98 μm, and the APS measures the coarse mode size distributions from 0.6 to 5.5 μm. We use the size distributions to identify the presence of aerosol dust layers. In many cases, these intense dust layers were visually identified by the instrument operators and in some cases specifically targeted by the DC-8 operators for sampling. Additional information about the composition of these layers is available from the NAMMA data archives (http://namma.msfc.nasa.gov/). For each size distribution sampled during a 5-second interval we fit the discrete measurements to the best continuous bimodal lognormal size distribution, as shown in Figure 1. The geometric mean radius and standard deviation of a fine and coarse mode derived from the in situ measurements are used in the numerical calculations.

On August 25, 2008, the DC-8 flew through a dense elevated dust layer measuring nearly 1 km in thickness at a mean altitude of about 2.3 km in an hour-long mostly straight and level flight. The APS and UHSAS measured coarse and fine size distributions, respectively, through the dust layer at intervals of 5 seconds. Figure 2 shows the probability distributions of the geometric mean fine and coarse radii of the dust layer. This figure is generated by taking the discrete 5-second size distribution measurements

209 and fitting these to a bimodal lognormal distribution as described above. For this dust
210 layer, the microphysical properties of mean, median, and standard deviations of the fine
211 (*coarse*) radius distributions, as shown in Figures 2 (a) and (b), are 0.059, 0.061, and
212 0.0064 μm (*0.54, 0.57, and 0.083 μm*), respectively. The mean, median, and standard
213 deviations shown in Figure 2 (c) and (d) for the fine (*coarse*) geometric standard
214 deviation distributions are 1.613, 1.630, and 0.101 (*1.495, 1.545, and 0.151*),
215 respectively.
216
217 The distributions in Figure 2 show that dust properties after lofting of these layers remain
218 relatively unchanged. Other studies [*Liu et al.*, 2008; *Maring et al.*, 2003; *Prospero and*
219 *Carlson*, 1971; 1972], have shown the same consistency in properties after long range
220 transport of dust. In each case, the means and medians of the size distribution descriptors
221 are close, i.e., the size descriptors are nearly normally distributed. The standard deviation
222 is a small fraction (<0.16) of the means, i.e., the variance of the data is small and thus the
223 layer is quite homogenous with respect to size across the 1 km vertical extent of the dust
224 plume.
225

226 **3.2. Scattering Models**

227 Mie scattering calculations [*Mie*, 1908], when applied to dust, are adequate for total
228 scattering, albedo and other flux related quantities, but result in large errors when used to
229 retrieve optical depth from satellite reflectance measurements. In particular and central to
230 the theme of this paper, are $S_a$ ratios calculated from measured size distributions. Mie
231 calculations underestimate $S_a$ by up to a factor of 2.0 leading to substantial errors in the

232 lidar derived aerosol optical depths [*Kalashnikova and Sokolik*, 2002]. This has been
233 known experimentally for quite some time: laboratory measurements by Perry et al
234 [1978] showed non-spherical particles, when compared to spherical particles having the
235 same equivalent volume, enhance side scattering and suppress backscattering. To account
236 for non-sphericity of dust particles, we use T-matrix calculations with the assumption that
237 the dust shapes can be modeled by randomly oriented prolate spheroids. T-Matrix is a
238 matrix formulation of electromagnetic scattering first proposed by *Waterman* [1971], and
239 subsequently improved and extended to much larger sizes and aspect ratios by *Mischenko*
240 *et al.* in a series of papers [*Mishchenko*, 1991; 1993; *Mishchenko and Travis*, 1994;
241 *Mishchenko et al.*, 1996a; *Mishchenko et al.*, 1996b; *Mishchenko and Travis*, 1998]. The
242 T-Matrix code used in these calculations is described in detail in *Mishchenko and Travis*
243 [1998]. This method is particularly suitable for light scattering calculations of non-
244 spherical, polydisperse, randomly oriented particles of identical axially symmetric shape
245 with size parameter, x ($x= \pi d_p/\lambda$; $d_p$ is particle diameter and $\lambda$ is the wavelength), smaller
246 than 30.
247
248 It is challenging to determine representative statistics of the mean shape for dust particles
249 because of their complexity and variety in shape. These particles are not only confined to
250 desert regions but are ubiquitous in continental areas where they contribute quite
251 significantly to the extinction budget [*Omar et al.*, 1999]. Fortunately, however,
252 randomly oriented prolate and oblate spheroids can adequately represent the scattering
253 properties of non-spherical particles of the same aspect ratio [cf. *Mischenko et al.*, 1995;
254 *Mishchenko and Travis*, 1994]. The aspect ratio is the ratio of the largest to the smallest

255 particle dimension. A prolate (oblate) spheroid is a rotationally symmetric ellipsoid with
256 a polar diameter greater (smaller) than the equatorial diameter.
257
258 There have been several studies of aspect ratio distributions representative of dust
259 aerosols. From an analysis of scanning electron microscope images of yellow sand
260 particles, Nakajima et al. [1989] found that the distribution of the minor to major particle
261 radius ratio peaked around 0.6, equivalent to an aspect ratio of 1.67. An investigation of
262 mineral dust particle shapes using electron microscopy by Okada et al. [1987] found a
263 mean aspect ratio of 1.4 ranging from 1.0 to 2.3. Hill et al [1984] compared the measured
264 scattering properties of 312 samples of soil dust with the simulated scattering properties
265 of randomly oriented prolate spheroids using T-matrix. They found the distributions of
266 the aspect ratio of prolate spheroids centered near 2.3 most closely reproduced the
267 measured scattering properties. For this study, we use a mean aspect ratio of 2.0 based on
268 the above studies and investigate the sensitivity of the $S_a$ ratio to aspect ratios ranging
269 from 1.7 to 2.3 partly to account for the dependence of the aspect ratio on size as
270 discussed by Kalashnikova and Sokolik [2004].
271
272 There is quite a wide range of estimated and measured mineral dust refractive indices (m-
273 ik). For wavelengths of 550 and 1000 nm, d'Almeida et al. [1991] estimate the real part
274 (m) of 1.53 and 1.52, respectively, and a spectrally invariant imaginary part (k) of 0.008
275 for dust-like aerosols, and 1.53-i0.0055 and 1.53-i0.001, respectively, for mineral dust.
276 Ackerman (1998) used values of 1.53-i0.0043 and 1.53-i0.0063 to calculate dust $S_a$ ratios
277 of 19-23 sr and 17-18 sr at 532 and 1064 nm, respectively. These values are much lower

than more recent 532-nm dust $S_a$ ratios of 40-60 sr [*Cattrall et al.*, 2005; *Di Iorio et al.*, 2003; *Muller et al.*, 2007; *Murayama et al.*, 2003; *Voss et al.*, 2001] because the Ackerman study assumed spherical particles.

Retrievals from radiances measured by ground-based Sun-sky scanning radiometers of the Aerosol Robotic Network (AERONET) over a 2-year period yielded dust complex refractive index values of 1.55 ± 0.03 – i0.0014 ± 0.001 at 670 nm and 1.55 ± 0.03-i0.001 ± 0.001 at 1020 nm at Bahrain (Persian Gulf), and 1.56 ± 0.03 – i0.0013 ± 0.001 at 670 nm and 1.56 ± 0.03-i0.001 ± 0.001 at 1020 nm at Solar Village in Saudi Arabia [*Dubovik et al.*, 2002]. Using vertically resolved aerosol size distributions in a scattering model constrained by lidar measurements of aerosol backscattering coefficient at 532 nm, Di Iorio et al. (2003) estimated dust refractive indices of 1.52 to 1.58 (real part), and 0.005 to 0.007 (imaginary part). Kalashnikova and Sokolik [2004] calculated effective refractive indices from component mixtures and found values of 1.61-i0.0213 and 1.59-i0.0032 for Saharan dust at wavelengths of 550 nm and 860 nm, respectively. The values for Asian dust, from the same monograph, are 1.51-i0.0021 and 1.51-i0.0007 at 550 nm and 860 nm, respectively. Using a twin angle optical counter , *Eidehammer et al.(2008)* estimated the indices of refraction to be in the range 1.60-1.67 for the real part and 0.009-0.0104 for the imaginary part.

The Saharan Mineral Dust Experiment [SAMUM, *Heintzenberg*, 2009; *Rodhe*, 2009] based in Morocco in 2006, produced several independent estimates of the complex refractive indices of Saharan dust. Kandler et al. [2009] determined Saharan dust aerosol complex refractive index from chemical/mineralogical composition of 1.55-i0.0028 and

301 1.57-i0.0037 at 530 nm for small (diameter < 500 nm) and large particles (diameter > 500
302 nm), respectively. Schladitz et al. [2009] derived mean refractive indices of 1.53 -
303 i0.0041 at 537 nm and 1.53 - i0.0031at 637 nm from measurements of scattering and
304 absorption coefficients, and particle size distributions. Using similar methods during
305 SAMUM, Petzold et al. [2009] found real parts of the refractive indices of Saharan dust
306 ranging from 1.55 to 1.56 and imaginary parts ranging from 0.0003 to 0.0052. Some of
307 the estimates of refractive indices reported in the literature are summarized in Table 1.
308

309 Table 1. Summary of complex dust refractive indices from previous studies

| Wavelength (nm) | Real Part | Imaginary Part | Source |
|---|---|---|---|
| 500 | 1.50 | 0.0045 | *Volz* [1973] |
| 1000 | 1.53 | 0.008 | *d'Almeida et al.* [1991], dust-like |
| 550 | 1.53 | 0.0055 | *d'Almeida et al.* [1991], mineral dust |
| 1000 | 1.53 | 0.001 | *d'Almeida et al.* [1991], mineral dust |
| 532 | 1.53 | 0.0043 | *Ackerman* [1998] dust |
| 1064 | 1.53 | 0.0063 | *Ackerman* [1998] dust |
| 670 | 1.55 ± 0.03 | 0.0014 ± 0.001 | *Dubovik et al.* [2002], Bahrain dust |
| 1020 | 1.55 ± 0.03 | 0.003 ± 0.001 | *Dubovik et al.* [2002], Bahrain dust |
| 670 | 1.56 ± 0.03 | 0.0013 ± 0.001 | *Dubovik et al.* [2002], Solar Village dust |
| 1020 | 1.56 ± 0.03 | 0.001 ± 0.001 | *Dubovik et al.* [2002], Solar Village dust |
| 532 | 1.52-1.58 | 0.005-0.007 | *Di Iorio et al.* [2003], Saharan dust |
| 500 | 1.42 | 0.003 | *Israelevich* [2003], Sede Boker dust |
| 860 | 1.51 | 0.0032 | *Kalashnikova and Sokolik* [2004] Saharan dust |
| 550 | 1.51 | 0.002 | *Kalashnikova and Sokolik* [2004] Asian dust |
| 860 | 1.51 | 0.0007 | *Kalashnikova and Sokolik* [2004] Asian dust |
| 670 | 1.45 | 0.0036 | *Omar et al.* [2005] dust cluster |
| 550 | 1.53 | 0.0015 | *Cattrall et al.*[2005] mineral dust |
| 1020 | 1.53 | 0.0005 | *Cattrall et al.* [2005] mineral dust |
| 300-700 | 1.60-1.67 | 0.009-0.0104 | *Eidehammer et al.* [2008] Wyoming dust |
| 537 | 1.53 | 0.0041 | *Schladitz et al.* [2009] Saharan dust |
| 637 | 1.53 | 0.0031 | *Schladitz et al.* [2009] Saharan dust |
| 450 | 1.55-1.56 | 0.0003-0.0052 | *Petzold et al.* [2009] Saharan dust |
| 700 | 1.55-1.56 | 0.0003-0.0025 | *Petzold et al.* [2009] Saharan dust |
| 530 | 1.55 | 0.0028-0.0037 | *Kandler et al.* [2009] Saharan dust |

310

311 To perform the sensitivity study described in section 6, we use values of the real part of

312 the refractive index ranging from 1.45 – 1.55 (normally distributed) and the imaginary

313 part ranging from 0.00067 – 0.006 (log normally distributed) with a central value of 1.50-
314 i0.002. For the scattering calculations using NAMMA size distributions, we use the
315 central values of the refractive indices along with the nearly instantaneous (5 second
316 interval) size distribution measurements to generate profiles of the aerosol properties.
317 Figure 3 is a plot of the fine mode, coarse mode, and total phase function of the dust
318 plume encountered on August 19, 2006. The fine mode and coarse mode phase functions
319 are computed from the mean of the instantaneous size distributions, and the total phase
320 function is the area-weighted composite of the fine and coarse mode phase functions. The
321 phase functions are driven largely by the coarse mode, especially at 532 nm, and exhibit a
322 more pronounced peak in the backscattering direction at 532 nm than 1064 nm
323

324 **4. Data Analyses of CALIPSO NAMMA Coincident Measurements**

325 For this study we analyzed coincident measurements of the CALIOP 532-nm extinction
326 profiles and in situ extinction profiles measured at wavelengths near the CALIOP green
327 channel. The in situ extinction coefficient is obtained by summing the scattering (550
328 nm) and absorption (532 nm) coefficients measured by a nephelometer and a PSAP,
329 respectively. Data from the nephelometer and PSAP have been corrected for errors
330 associated with the limited detector viewing angle [*Anderson and Ogren*, 1998] and
331 scattering from the filter media [*Virkkula et al.*, 2005], respectively. We make the
332 assumption that the scattering properties are invariant over the 532 – 550 nm range for
333 these large dust particle sizes. We chose three days on which there were near collocated
334 CALIPSO and NAMMA measurements of nearly the same airmass.

### 4.1. August 19, 2006 NAMMA Flight 4

August 19 was one of the days the DC-8 performed an under flight of CALIPSO. Figure 4 shows the time-altitude flight track of the DC-8. A nearly coincident in-situ profile was obtained during the second ascent leg shown in the figure. Atmospheric context for this flight is given by Figure 5(a) and (b), in which both the DC-8 and CALIPSO flight tracks are superimposed on images of measurements made by the Moderate Resolution Imaging Spectroradiometer (MODIS) and Measurements of Pollution in the Troposphere (MOPITT), respectively. The DC-8 flight tracks are the black irregular octagons and the CALIPSO orbit tracks are the straight lines in both images. The underflights in the figures are segments where the DC-8 flight tracks are nearly exactly collocated and parallel to the CALIPSO flight tracks. The MODIS optical depth near the coincident flight segment is about 0.5. The MOPPITT image shows moderate CO concentrations in the vicinity of the coincident flight track and therefore indicates that most of the aerosol is dust and not continental pollution or biomass burning. This can also be confirmed by the CALIPSO depolarization measurements. The image also shows high CO concentrations ($>2.5 \times 10^{18}$ molecules/cm$^2$) to the south of the DC-8 flight tracks most likely due to biomass burning, and identified as such by the CALIPSO aerosol subtyping scheme illustrated later in this section.

Unfortunately, the direct underflight of CALIPSO by the DC-8 was a nearly level flight with no in situ profile information. In fact the DC-8 was at a high altitude near Flight Level 330 (~ 10 km) throughout the underflight and therefore did not encounter any significant aerosol layer at this altitude to sample. We used the ascending leg of the DC-8

358 flight which corresponds to the flight segment during ascent to the CALIPSO underflight
359 portion denoted by blue dots in Fig 5a. The in situ profiles segment is shown in Fig. 4.
360 The CALIPSO browse images (e.g., Fig. 6) are plots of the attenuated backscatter color
361 coded by intensity varying from blue (weak) to white (very strong). A horizontal line
362 near the 0 km mark denotes the surface. The CALIPSO data used for comparison with the
363 in-situ data come from the 80 profiles (~27 km horizontal average) between the white
364 lines in the browse image (Fig. 6). To determine the optimal 532-nm $S_a$ ratio for these
365 data, we iteratively adjust $S_a$ until the difference, in a least squares sense, between the
366 retrieved CALIPSO profile, $\sigma_{a,532\text{-nm}}$, and the measured NAMMA profile, $\sigma_{a,550\text{-nm}}$, is
367 minimized.
368
369 Figure 7 is a plot of the extinction profiles retrieved from CALIPSO's 532-nm
370 backscatter profiles and the profiles of the sum of scattering (550 nm) and absorption
371 (532 nm) measured by the nephelometer and the PSAP aboard the NASA DC-8,
372 respectively. These profiles were taken during the ascent leg shown in Figure 4
373 corresponding to the flight tracks shown in Figure 5(a). The boundary between the two
374 layers is determined by the increase in the extinction coefficient near 2 km. The two $S_a$
375 ratios are values that provide the best fit in a least squares sense of the CALIPSO data to
376 the NAMMA in-situ measurements. The 532-nm $S_a$ ratios are consistent with a dust
377 plume ($S_a$ = 35.7 sr) above seasalt in the marine boundary layer ($S_a$ = 25 sr). The root
378 mean square (rms) of the differences between the CALIPSO and the NAMMA in-situ
379 extinction coefficient profiles are 20.2 $Mm^{-1}$, and 47.4 $Mm^{-1}$, for the marine and dust
380 layers, respectively. The rms of the differences in the extinction coefficients in the clear

region (4 to 8.5 km) above the dust layer in Fig. 6 is 12.3 $Mm^{-1}$. We see some differences in the two extinction profiles in Figure 7 likely due to the temporal and spatial differences of 30 minutes and 160 km, respectively, between DC-8 and CALIPSO.

Figure 8 is an image of the aerosol scattering ratios measured by the Lidar Atmospheric Sensing Experiment (LASE) on board the DC-8 during the ascent leg of Flight 4 on August 19, 2006 as indicated in Figure 4. The measurements were made at 815 nm and the extinction calculation was performed using an $S_a$ ratio of 36 sr [*Ismail et al.*, 2010]. The DC-8 flight track is shown by the solid line in Figure 8 during which the in-situ measurements shown in Figure 7 were made. The figure also shows the region nearest to the CALIPSO overpass where measurements of the CALIPSO profiles shown in Figure 7 were made. LASE also observed a dust layer extending to an altitude of 6 km at the coincident point. This dust layer is optically and geometrically thick, and is lofted over a layer of lower optical depth (aerosol scattering ratio ~ 1) in the marine boundary layer. Some differences in altitude and extent of the layer between the CALIPSO and LASE measurements can be attributed to temporal and spatial mismatch.

Figure 9 is a plot of the results of (a) the cloud-aerosol discrimination and (b) aerosol classification algorithms applied to the data shown in the browse image including the NAMMA underflight (Flight 4 of August 19, 2006). The CALIPSO level 2 algorithms first discriminate between aerosol and clouds [*Liu et al.*, 2009] and then classify the aerosol layers into aerosol subtypes [*Omar et al.*, 2009]. Figure 9(a) shows that some of the optically thick aerosol near $15^{o}$ N was misclassified as clouds, and thus was not

404 examined by the aerosol subtyping algorithm. The presence of biomass burning smoke
405 and polluted dust (mixture of dust and smoke) during the first part of the flight depicted
406 in Figure 9(b) is borne out by the high CO concentrations in the MOPPITT data to the
407 south of the DC-8 flight tracks shown in Figure 5(b). Though the small lump of aerosol at
408 the surface near $15^{o}$ N is classified as pure dust, it is more likely a mixture of dust and
409 marine aerosol. The white line in the Figure is the midpoint of the 80 profiles averaged
410 for the retrieval of the extinction profile discussed above.
411
412 CALIPSO also measured a dense Saharan dust layer to the southwest of the coincident
413 measurements during a nighttime orbit on the same day (August 19, 2006). The browse
414 images of attenuated backscatter at 532 nm for this measurement are shown in Figure 10.
415 The inset map in Figure 10 shows the CALIPSO ground track in blue. This dust layer
416 appears to be a more robust part of the same dust plume observed during the coincident
417 measurement.
418
419 As shown (by the red dotted oval) in Figure 10(a), the layer exceeds 1000 km in
420 horizontal extent (from 18.3N to 10.3N). The 532-nm aerosol optical depth (AOD) is
421 greater than about 0.3 across most of the 1000-km orbital segment shown in Figure 10(a).
422 Figure 10(b) is a magnified illustration of the region in 9(a) subtended by the yellow
423 dotted line. We divided the layer into five segments and applied the transmittance method
424 of section 2.1 to calculate a 532-nm $S_a$ and the 2-color method of section 2.2 to calculate
425 a 1064-nm $S_a$ ratio. These values are shown in green (532 nm) and red (1064 nm) in
426 Figure 10(b). Clear air regions above and below each dust layer were identified

427 manually, by inspection of the profiles. Note that for this mesoscale layer the 532-nm $S_a$
428 ratios range from 38 to 41 sr with an average of 40.1 sr and the 1064-nm $S_a$ ratios range
429 from 45.8 to 54.2 with an average of 50.9 sr.
430
431 Figure 10 shows that the Sahara dust layers once elevated are consistent both
432 geometrically (the layer is confined to 3-5 km altitude band) and optically ($S_a$ variation at
433 both wavelengths is small and the layer optical depth is near 0.3). The $S_a$ ratio is an
434 intensive aerosol property that depends on the composition, size distributions, and
435 particle shape of the aerosol and its consistency is an indication that these layers stay
436 intact over very long distances. Other studies have shown the transport of relatively
437 unmixed Saharan mineral dust to the south American rainforest [*Ansmann et al.*, 2009;
438 *Graham et al.*, 2003] and western Atlantic Ocean [*Formenti et al.*, 2003; *Kaufman et al.*,
439 2005], including the US eastern seaboard (cf. *Liu et al. 2008*).

440 **4.2. August 26, 2006**

441 The August 26 DC-8 flight included an underflight of CALIPSO. As is the case with the
442 coincident CALIPSO-NAMMA measurements on August 19, the collocated
443 measurements are at one level and lack in-situ profile measurements. In situ profiles of
444 the size distributions were estimated from the DC-8 data obtained during the descent
445 flight segment shown by a red dashed tilted oval in Figure 11 (a) and flown about two
446 hours earlier than the CALIPSO underflight. The MOPITT CO levels (Figure 11b) for
447 this period are slightly elevated. The extinction comparison shows that the layer observed
448 by CALIPSO is more elevated than the one encountered by the DC-8. Figure 12 is a
449 browse image of the CALIPSO 532-nm attenuated backscatter coefficients measured

450 during the orbital segment corresponding to Flight 8 of the DC-8. The CALIPSO data
451 used for comparison with the in-situ extinction profiles were extracted from the region
452 between the two white lines shown in the figure.
453
454 Figure 13 compares the CALIPSO extinction profile with a profile of the extinction
455 derived from in situ measurements (i.e., the sum of the absorption and scattering
456 coefficients). The maximum extinction coefficients (160 and 140 $Mm^{-1}$ by CALIPSO and
457 the DC-8, respectively) are comparable, showing that the layer is intact after two hours.
458 The altitudes of the maximum layer extinctions for the CALIPSO and NAMMA
459 measurements are offset by at least one kilometer. The in situ measurements and
460 CALIPSO observations are far removed from each other in this case (two hours and 1250
461 km). The data shown in Figure 12 is north of the NAMMA flight segment. These
462 differences are shown by the mismatch in layer heights shown in Figure 13. Because of
463 the relatively large mismatch, the constraint method, which requires good coincidence, is
464 not applicable to this case to derive $S_a$. However, the transmittance technique can be
465 applied using the CALIPSO measurement averaged over the region bounded by two
466 white lines in Figure 12. Note that the dust layer overlies a streak of marine stratus just
467 above the marine boundary layer. At 532 nm, the dust layer has an optical thickness of
468 0.41 and an $S_a$ ratio of 38.2 sr. Though the Saharan layers can have horizontal extents of
469 thousands of km, it is possible that the layer observed by CALIPSO is not the same as the
470 one measured by the in situ instruments aboard the DC-8. Notwithstanding this
471 possibility, the properties measured by the two methods provide independent
472 characterization of the Saharan dust layer(s).

473

474 **4.3. September 1, 2006**

475 Flight 10 of the DC-8 on September 1, 2006 neither directly underflew nor intercepted
476 the CALIPSO orbit tracks. However, this flight sampled some of the same aerosol layers
477 measured during a CALIPSO orbit track, as shown in the MODIS aerosol optical depth
478 image in Figure 14(a). The region of interest is denoted by the red circle. The DC-8 flight
479 segment most relevant and of closest proximity is the descending leg located in this
480 region. The MOPPITT CO concentrations are low (1.5 - 2 x $10^{18}$ molecules/$cm^2$) in the
481 comparison region. It is therefore likely that most of the aerosol mass is Saharan dust.
482 CALIPSO preceded the DC-8 by 14 hours. As in the previous flight of August 26, the
483 observed layers by CALIPSO and the in situ measurements may be different.
484
485 The CALIPSO browse image (Figure 15) shows the layers of interest marked by two
486 white lines and comprising of 80 profiles. The MOPITT image of this area shows no
487 enhancement of CO in the sampling region subtended by a red circle in Figure 14(a). The
488 transmittance and 2-color methods yielded $S_a$ ratios of 39.8 sr and 56 sr at 532 nm and
489 1064 nm, respectively. The optical depth determined from the inversion of the CALIOP
490 attenuated backscatter using this lidar ratio (39.8 sr at 532 nm) is 0.55. In Figure 14(a),
491 the MODIS AOD is about 0.5 in this region.
492
493 It is a general transport pattern that Saharan dust aerosol goes through a phase of rising
494 motion near the source then relative horizontal transport culminating in descent and
495 deposition near the Americas [*Ansmann et al.*, 2009; *Formenti et al.*, 2003; *Graham et*

496 *al.*, 2003; *Kaufman et al.*, 2005; *Okin et al.*, 2004]. If the layer observed on September 1,
497 2006 by CALIPSO is the same as the one observed by the in situ measurements, then it
498 was in the rising phase at a rate of approximately 0.1 kilometers per hour. The rate of
499 ascent is based on the time difference between the CALIPSO overpass (3:30 am Local
500 Time) and DC-8 flight track (6:30 pm Local Time) of nearest approach. The extinction
501 profiles' comparison (Figure 16) between the DC-8 in-situ measurements and the
502 CALIPSO measurements shows an offset of 1.5 km in the altitude of maximum
503 extinction coefficient. The layer shown at the same location has been elevated by 1.5 km
504 since CALIPSO sampled it. During this rising phase, there is no evidence of significant
505 deposition, since the maximum extinction coefficient, a property of the aerosol loading,
506 does not decay appreciably.
507
508 **5. Extinction-to-backscatter ($S_a$)ratios calculation based on NAMMA in situ**
509 **measurements**
510 To determine profiles of $S_a$ ratios and validate the retrieved values, we perform numerical
511 calculations for Saharan dust based on NAMMA in-situ size distribution measurements.
512 We use the DC-8 APS and UHSAS measurements (Chen et al., 2010) to determine coarse
513 and fine size distributions, and then calculate coarse and fine mode phase functions, as in
514 Figure 3, using a T-Matrix scheme. The $S_a$ ratio of the aerosol is derived from an area-
515 weighted integral of the two modes. Figure 17 is a plot of the profile of $S_a$ ratios of the 2-
516 km dust layer encountered by NAMMA Flight 4 on August 19, 2006. The figure shows a
517 profile of the coarse number concentration which marks the bottom and top of the layer at
518 2.5 and 4.6 km, respectively. This is very similar to the coincident CALIPSO extinction

519 profile shown in Figure 7. The 532-nm and 1064-nm $S_a$ ratios calculated by this method
520 are 34.3 ± 2.0 sr and 50.2 ± 5.7 sr, respectively. These are in good agreement with $S_a$
521 ratios of 38 to 41 sr at 532 nm and 45.8 to 54.2 sr at 1064 nm independently determined
522 from CALIPSO measurements using the transmittance technique (Figure 10) on the same
523 day, albeit further downfield.
524 Part of the flight on August 25, 2006 was dedicated to an intercomparison of the in situ
525 measurements on the NASA DC-8 and the British BAe146. The DC-8 made a nearly
526 straight and level flight through a dust cloud near 2 km. Figure 18 (a) and (b) show the
527 DC-8 altitudinal flight tracks, and the calculated $S_a$ ratios (and the coarse number
528 concentration) for this flight, respectively. The dust layer is quite tenuous with maximum
529 coarse number concentrations ~ 20 $cm^{-3}$. Scattering coefficients varied from 50 to 75
530 $Mm^{-1}$ on intercomparison legs near 19 deg N latitude. Condensation Nuclei (CN)
531 concentrations in the dust layers were fairly low, around 300 $cm^{-3}$, while CO mixing
532 ratios were ~85 ppbv and RH was ~50 to 60%. Both the CCN and CO concentrations
533 infer the predominance of dust in the aerosol layer. The profiles of the 532- and 1064-nm
534 $S_a$ ratios shown in Figure 18 for this dust layer are quite consistent with means of 38.0 ±
535 2.5 sr, and 48.7 ± 3.2 sr, respectively. The small standard deviations in both $S_a$ ratios
536 indicate that the layer remains very uniform with respect to this optical property.
537
538 Size distribution measurements were made during the NAMMA DC-8 Flight 8 on August
539 26, 2006 of a low density dust layer between 0.6 and 1.6 km. Profiles of $S_a$ ratios
540 calculated from these measurements are shown in Figure 19. The calculated values are
541 39.0 ± 1.5 sr and 45.9 ± 2.2 sr at 532-, and 1064-nm, respectively.

This layer is optically thinner than the dust layer encountered on August 19, 2006. Nevertheless, the $S_a$ ratios determined by T-Matrix calculation for this layer and the direct measurement for the denser layer on August 19, 2006 (40.1 and 50.9 sr at 532 and 1064 nm, respectively) are quite close. The calculated $S_a$ ratio at 532 nm is also consistent with the value (38.2 sr) retrieved from the CALIPSO measurements on the same day.

During the return flight on August 26, 2006, the DC-8 performed a stair-step descent flight consisting of two level sections and two descent sections. The first straight and level section (Leg 1 in Figure 20a.) was flown at an altitude of ~2.25 km in a dense dust plume with coarse number concentrations near 35 particles $cm^{-3}$. The mean $S_a$ ratios are 42.4 ± 1.3 and 53.3 ± 2.0 sr at 532 nm and 1064 nm, respectively. The plume is fairly consistent as shown by the small standard deviations in the $S_a$ ratios at both wavelengths. Fig. 20(b) are profile plots of the two descent legs (leg 2 and 4 shown in plot (a) the flight path). The break in ordinate demarcates the straight and level section (leg 3) of the flight. The 532 nm and 1064 nm $S_a$ ratios for leg 2 are 46.6 ± 1.3 sr, and 52.6 ± 1.7 sr, respectively. In leg 4, the aircraft has begun its descent into the marine boundary layer and there is a sharp decline in the coarse number concentration. The $S_a$ ratio at 532 nm has also dropped considerably signifying a change in the aerosol composition. The calculated $S_a$ ratios for leg 4 are 32.8 ± 1.5 sr, and 51.4 ± 10.8 sr, at 532 and 1064 nm, respectively. Note that for leg 4, the 532 nm $S_a$ ratios are fairly consistent while the 1064 nm values are quite noisy and decrease at lower altitudes. The decreasing trend in lidar ratios at 1064 nm with altitude corresponds to a decrease in the aerosol coarse mode number concentration.

565 Figure 21 shows the flight path for the in-situ measurements on August 20, 2006. The
566 time is in seconds after midnight UTC. Plot (b) shows a profile plot of the 532 nm and
567 1064 nm $S_a$ ratios observed during the descent phase through a dust layer extending from
568 an altitude of 1.6 km to 4.8 km. The 532 nm and 1064 nm $S_a$ ratios for this dust layer are
569 40.8 ± 3.2 sr, and 51.6 ± 3.8 sr, respectively. Plot (c) shows the profiles of the 532 nm
570 and 1064 nm $S_a$ ratios observed during the ascent phase through the dust layer. The 532-
571 nm and 1064-nm $S_a$ ratios for this dust layer are 42.8 ± 3.0 sr, and 51.8 ± 3.4 sr,
572 respectively. The similarity of the vertical extent and the $S_a$ ratios at each wavelength
573 suggests that the same dust layer was sampled during both the ascent and descent legs of
574 the flight. As noted before, these layers have spatially and temporally uniform $S_a$ ratios
575 and perhaps by inference, fairly constant compositions, and are geometrically quite
576 stable.
577
578 Figure 22 is a histogram of all the 532-nm and 1064-nm $S_a$ ratios (~1100 points)
579 determined using the size distributions measured during NAMMA for this study. There is
580 very little overlap of the two nearly normally distributed $S_a$ ratios. The 532-and 1064-nm
581 mean $S_a$ ratios (± one standard deviation) are 39.1 ± 3.5 sr and 50.0 ± 4.0 sr, respectively.
582 The 532-nm values ranged from 30 to 53 sr and the 1064-nm values ranged from 32 to 66
583 sr, in both cases within the estimated ranges of 10 – 110 sr for all aerosol types
584 [*Ackermann*, 1998; *Anderson et al.*, 2000; *Barnaba and Gobbi*, 2004]. Figure 23 is a plot
585 of the frequency distribution of the ratio of $S_a$ ratios, i.e., $S_a$ (1064 nm) /$S_a$ (532 nm), a
586 parameter used in the lidar ratio determination scheme outlined in Cattrall et al. (2005).
587 The plot shows that for the Sahara dust sampled during NAMMA there is very little

588 spread in the ratio of $S_a$ values. The mean 1064 nm $S_a$ ratio is about 30% larger than the
589 mean 532 nm value for this Saharan dust with a standard deviation of 10%, i.e., $S_a$ (1064
590 nm) /$S_a$ (532 nm) = 1.3 ± 0.13. Since the $S_a$ ratio is an intensive property of the aerosol,
591 its ratio is also an intensive property. The small spread in the ratios of $S_a$ denotes that the
592 Saharan dust aerosol observed during this period is quite consistent at least in its size
593 distributions. To explore the effects of varying composition (refractive indices) and shape
594 (aspect ratios) on the T-Matrix calculations, both of which were not directly measured for
595 this study, we use the uncertainty analysis described in the next section.
596 Table 2 summarizes the $S_a$ ratios obtained for Saharan dust aerosols during NAMMA
597 using the three methods. The 532-nm values are fairly consistent while there is a
598 somewhat wider spread in the 1064-nm values. This is particularly interesting because
599 these measurements were made on various days and at various locations.
600
601

602 Table 2. Summary of $S_a$ ratio measurements and calculations

| | $S_a$ (532 nm) sr | $S_a$ (1064 nm) sr |
|---|---|---|
| Constrained method | | |
| 08/19/2006 | 35.7 | NA |
| Transmittance + 2-color methods | | |
| 08/19/2006 | 38.9 | 53.5 |
| 08/19/2006 | 41.4 | 50.9 |
| 08/19/2006 | 38.1 | 54.2 |
| 08/19/2006 | 41.0 | 45.8 |
| 08/19/2006 | 41.0 | 50.2 |
| 08/26/2006 | 38.2 | NA |
| 09/01/2006 | 39.8 | 56.0 |
| Mean | 39.8 ± 1.4 | 51.8 ± 3.6 |
| T-Matrix using NAMMA size distribution measurements | | |
| 08/19/2006 | 34.3 ± 2.0 | 50.2 ± 5.7 |
| 08/25/2006 | 38.0 ± 2.5 | 48.7 ± 3.2 |
| 08/26/2006 | 39.0 ± 1.5 | 45.9 ± 2.2 |
| 08/26/2006 | 42.4 ± 1.3 | 53.3 ± 2.0 |
| 08/26/2006 | 46.6 ± 1.3 | 52.6 ± 1.7 |
| 08/26/2006 | 32.8 ± 1.5 | 51.4 ± 10.8 |
| 08/20/2006 | 40.8 ± 3.2 | 51.8 ± 3.4 |
| 08/20/2006 | 42.8 ± 3.0 | 51.8 ± 3.4 |
| Mean | 39.1 ± 3.5 | 50.0 ± 4.0 |
| Noise Laden T- Matrix Simulation | | |
| Mean | 39.4 ± 5.9 | 56.5 ± 16.5 |

603

604
605

606 **6. Uncertainty Analysis of the modeled $S_a$ ratios**

607 In this section we attempt to propagate the uncertainty in the input variables to the
608 calculated $S_a$ ratio and determine the overall uncertainty in the calculated dust 532-nm
609 and 1064-nm $S_a$ ratios using a generalized analytical uncertainty equation. The
610 uncertainty equation is given by the Taylor series of the deviations $(y - y^o)$ of the output
611 (y) from its nominal value ($y^o$) and is expressed in terms of the deviations of the i inputs
612 $(x - x_i^o)$ from their nominal values. As in Morgan and Henrion [1990], for the first three
613 terms, the uncertainty is,

614

615
$$y - y^o = \sum_{i=1}^{N} (x_i - x_i^o) \left.\frac{\partial y}{\partial x_i}\right|_{X^o} + \qquad \text{I}$$
$$\frac{1}{2}\sum_{i=1}^{N}\sum_{j=1}^{N} (x_i - x_i^o)(x_j - x_j^o) \left.\frac{\partial^2 y}{\partial x_i \partial x_j}\right|_{X^o} + \qquad \text{II} \qquad (5)$$
$$\frac{1}{3!}\sum_{i=1}^{N}\sum_{j=1}^{N}\sum_{k=1}^{N} (x_i - x_i^o)(x_j - x_j^o)(x_k - x_k^o) \left.\frac{\partial^3 y}{\partial x_i \partial x_j \partial x_k}\right|_{X^o} + \ldots \qquad \text{III}$$

616

617 The subscripts $X^o$ denote derivatives evaluated at the nominal values. Assuming that
618 there are no covariances between the input variables, all the mixed derivatives in eq. (5)
619 would equal zero. The only terms that would not be zero are the first term and the terms
620 with i= j and i = j = k in summations II and III, i.e., second and third derivatives of the
621 variables, respectively. Since the covariances are not known we cannot make the
622 assumption that they are negligible. Given the uncertainties in the variables from which
623 the $S_a$ ratio is calculated, the uncertainty in $S_a$ can be estimated without making any
624 assumptions about covariances between inputs. To accomplish this we use Latin

625 Hypercube Sampling [LHS, *Iman and Conover*, 1980], a statistical sampling method in
626 which a distribution of plausible scenarios of parameter values is generated from a
627 multidimensional distribution. Unlike classical Monte Carlo sampling methods, LHS
628 precludes duplication by requiring that each square grid containing sample positions has
629 only one sample in each row and each column. For this study, we generate 500 variables
630 for each of the seven uncertain parameters used in the calculation of $S_a$. We then
631 randomly combine these variables to yield 500 instances or events. Each of these events
632 has a very high probability of yielding a unique $S_a$ ratio. We then perform standard
633 descriptive statistics on the $S_a$ values.
634
635 The mean and standard deviations of these values is an estimate of the nominal value and
636 uncertainty of dust $S_a$. We use the nominal (or central) values in Table 3, suggested by
637 the studies referenced in section 2, to generate the random scenarios. The fine mode radii,
638 coarse mode radii, and imaginary refractive indices are log normally distributed. The fine
639 and coarse geometric standard deviations (GSD), the real refractive indices, and the
640 aspect ratios are normally distributed.
641
642 The results obtained by using this method do not assume that the input variables are
643 independent of each other or that $S_a$ ratio is linear in the individual input variables, i.e.,
644 the second- and higher-order derivatives in Equation 5 are not necessarily equal to zero.
645 The statistics of the resulting $S_a$ ratios provide an uncertainty envelop of the $S_a$ ratio
646 estimates based on the uncertainty of the inputs. Moreover, the results can be used to
647 explore the sensitivity of the $S_a$ ratios at each wavelength to the various aerosol

properties. In Figure 24, the 532-nm $S_a$ ratios are well constrained with a standard deviation of 15% of the mean after perturbing nominal input values shown in Table 3 and similar to the distribution shown in Figure 22. The 1064-nm $S_a$ ratios are much more sensitive to the addition of noise as shown by the wide spread of 1064-nm $S_a$ ratios in Figure 24. A parameter that has a significant impact on the $S_a$ ratios is the complex refractive index. Figure 25 is a 2-D histogram of the 532- and 1064-nm $S_a$ ratios as functions of the real and imaginary parts of the refractive indices. The range of these values is from 0.00067 to 0.006 for the imaginary part and 1.45 to 1.55 for the real part. The 1064-nm $S_a$ ratios are sensitive to changes in the refractive index throughout the ranges of these variables. The 532-nm $S_a$ ratio is sensitive to changes in the complex refractive index at the lower ranges (Figures 25a and 25c). The highest density of 532-nm $S_a$ ratios are found in midranges of both the real and imaginary part, and these values are insensitive to changes in the complex refractive index. Note that this variation is a total derivative, i.e., all parameters are allowed to vary independently for the scenarios. The 1064-nm $S_a$ ratios decrease with the complex index of refraction almost monotonically through the range of values (Figures 25b and 25d)

666 Table 3. Ranges of the variables used to generate 500 random combinations of inputs for
667 T-Matrix calculations. The central values of the size distributions are based on the mean
668 values of the dust layer observed on 08/19/2006 during the NAMMA campaign
669

| Parameter | Minimum | Maximum |
|---|---|---|
| Geometric Fine Radius | 0.0216 | 0.194 |
| Geometric Coarse Radius | 0.188 | 1.69 |
| Fine GSD | 1.60 | 1.80 |
| Coarse GSD | 1.50 | 1.70 |
| Real Refractive Index | 1.45 | 1.55 |
| Imaginary Refractive Index | 0.00067 | 0.006 |
| Aspect Ratio | 1.70 | 2.30 |

670

671 **7. Conclusion**

672 We have determined the $S_a$ ratios of Saharan dust layers using three methods:
673 transmittance constraint technique for lofted layers, in-situ extinction profile constraint
674 method, and T-Matrix calculations. We found quite robust $S_a$ ratios at 532 nm and a
675 slightly wider spread at 1064 nm. The three methods yielded 532 nm and 1064 nm $S_a$
676 ratios that are quite close. $S_a$ ratios of 39.8 ± 1.4 sr and 51.8 ± 3.6 sr at 532 nm and 1064
677 nm, respectively, were produced using the transmittance and 2-color methods applied to
678 CALIPSO measurements of Saharan dust lofted layers. T-Matrix calculations applied to
679 size distributions measured aboard the NASA DC-8 during NAMMA yielded $S_a$ ratios of
680 39.1 ± 3.5 sr and 50.0 ± 4 sr at 532 nm and 1064 nm, respectively. The measured
681 extinction profile obtained by the aggregate of nephelometer measurements of total

682 scattering coefficient and the PSAP measurements of the absorption coefficient was used
683 to constrain the inversion of the CALIPSO measurements. This technique yielded a 532-
684 nm $S_a$ ratio of 35.7 sr for a dust layer and 25 sr for the aerosol in the marine boundary
685 layer. We perturbed seven microphysical and chemical properties of the dust aerosol and
686 computed the $S_a$ ratios by randomly combining distributions of these parameters to assess
687 the uncertainty in the $S_a$ calculation. This uncertainty simulation generated a mean (±
688 uncertainty) $S_a$ of 39.4 (± 5.9) sr and 56.5 (± 16.5) sr at 532 nm and 1064 nm,
689 respectively, corresponding to percent uncertainties of 15% and 29%. The ratio of the $S_a$
690 ratios, $S_a$ (1064 nm) /$S_a$ (532 nm) = 1.3 ± 0.13, and nearly normally distributed. The
691 simulation revealed that $S_a$ is insensitive to the middle range of refractive indices at 532
692 nm and nearly monotonically dependent on the refractive indices at 1064 nm. This
693 explains the observed robust $S_a$ ratios at 532 nm and relatively wide spread of $S_a$ at 1064
694 nm
695 This study examined a wide range of dust loadings in various locations within ~1250 km
696 of Saharan Desert source regions on different days. The $S_a$ ratios do not change
697 significantly with dust loading, suggesting the dust microphysical and chemical
698 properties do not vary appreciably. The profile of $S_a$ ratios at 532 nm are very close to 40
699 sr using different methods and on different days. There is a wider variation in the 1064
700 nm $S_a$ ratios for all methods. It is possible that the variation of $S_a$ at 1064 nm is driven by
701 a higher sensitivity to changes in the complex index of refraction at the 1064 nm
702 wavelength. The ratio of $S_a$ ratios at the two wavelengths [$S_a$ (1064 nm)/$S_a$ (532 nm)] is
703 1.3 ± 0.13.

## 8. Acknowledgements

We gratefully acknowledge funding support from the NASA Radiation Sciences and Atmospheric Composition Programs, respectively managed by Drs. Hal Maring and Bruce Doddridge, and the CALIPSO team for the satellite data and many discussions

## 9. References


Ackermann, J. (1998), The extinction-to-backscatter ratio of tropospheric aerosol: A numerical study, *J. Atmos. Ocean Tech.*, *15*, 1043-1050.

Anderson, T. L., and J. A. Ogren (1998), Determining aerosol radiative properties using the TSI 3563 integrating nephelometer, *Aerosol Sci. Technol.*, *29*(1), 57-69.

Anderson, T. L., S. J. Masonis, D. S. Covert, and R. J. Charlson (2000), In situ measurements of the aerosol extinction-to-backscatter ratio at a polluted continental site, *J. Geophys. Res.*, *105*(D22), 26907-26915.

Ansmann, A., H. Baars, M. Tesche, D. Muller, D. Althausen, R. Engelmann, T. Pauliquevis, and P. Artaxo (2009), Dust and smoke transport from Africa to South America: Lidar profiling over Cape Verde and the Amazon rainforest, *Geophysical Research Letters*, *36*, 5.

Barnaba, F., and G. P. Gobbi (2004), Modeling the aerosol extinction versus backscatter relationship for lidar applications: Maritime and continental conditions, *J. Atmos. Ocean Tech.*, *21*(3), 428-442.

Berthier, S., P. Chazette, P. Couvert, J. Pelon, F. Dulac, F. Thieuleux, C. Moulin, and T. Pain (2006), Desert dust aerosol columnar properties over ocean and continental Africa from Lidar in-Space Technology Experiment (LITE) and Meteosat synergy, *J. Geophys. Res.-Atmos.*, *111*(D21), 20.

Cattrall, C., J. Reagan, K. Thome, and O. Dubovik (2005), Variability of aerosol and spectral lidar and backscatter and extinction ratios of key aerosol types derived from selected Aerosol Robotic Network locations, *J. Geophys. Res.*, *110*(D10).

Chen, G., L. D. Ziemba, D. A. Chu, K. L. Thornhill, G. L. Schuster, E. L. Winstead, G. S. Diskin, R. A. Ferrare, S. P. Burton, S. Ismail, S. A. Kooi, A. H. Omar, D. L. Slusher, M. M. Kleb, C. H. Twohy, and B. E. Anderson (2010), Observations of Saharan Dust Microphysical and Optical Properties from the Eastern Atlantic during NAMMA Airborne Field Campaign, *Atmos. Chem. Phys.*, *(submitted)*.

d'Almeida, G. A., P. Koepke, and E. P. Shettle (1991), *Atmospheric Aerosols: Global Climatology and Radiative Characteristics*, A. Deepak Publishing, Hampton, VA.

DeMott, P. J., K. Sassen, M. R. Poellot, D. Baumgardner, D. C. Rogers, S. D. Brooks, A. J. Prenni, and S. M. Kreidenweis (2003), African dust aerosols as atmospheric ice nuclei, *Geophysical Research Letters*, *30*(14).

751 Di Iorio, T., A. di Sarra, W. Junkermann, M. Cacciani, G. Fiocco, and D. Fua (2003),
752 Tropospheric aerosols in the Mediterranean: 1. Microphysical and optical properties, *J.*
753 *Geophys. Res.*, *108*(D10).
754
755 Di Iorio, T., A. di Sarra, D. M. Sferlazzo, M. Cacciani, D. Meloni, F. Monteleone, D.
756 Fua, and G. Fiocco (2009), Seasonal evolution of the tropospheric aerosol vertical profile
757 in the central Mediterranean and role of desert dust, *J. Geophys. Res.-Atmos.*, *114*, 9.
758
759 Dubovik, O., B. N. Holben, T. F. Eck, A. Smirnov, Y. J. Kaufman, M. D. King, D. Tanre,
760 and I. Slutsker (2002), Variability of absorption and optical properties of key aerosol
761 types observed in worldwide locations, *J. Atmos. Sci.*, *59*, 590-608.
762
763 Dunion, J. P., and C. S. Velden (2004), The impact of the Saharan air layer on Atlantic
764 tropical cyclone activity, *Bulletin of the American Meteorological Society*, *85*(3), 353-+.
765
766 Eidhammer, T., D. C. Montague, and T. Deshler (2008), Determination of index of
767 refraction and size of supermicrometer particles from light scattering measurements at
768 two angles, *J. Geophys. Res.-Atmos.*, *113*(D16), 19.
769
770 Formenti, P., W. Elbert, W. Maenhaut, J. Haywood, and M. O. Andreae (2003),
771 Chemical composition of mineral dust aerosol during the Saharan Dust Experiment
772 (SHADE) airborne campaign in the Cape Verde region, September 2000, *J. Geophys.*
773 *Res.-Atmos.*, *108*(D18).
774
775 Graham, B., P. Guyon, W. Maenhaut, P. E. Taylor, M. Ebert, S. Matthias-Maser, O. L.
776 Mayol-Bracero, R. H. M. Godoi, P. Artaxo, F. X. Meixner, M. A. L. Moura, C. Rocha, R.
777 Van Grieken, M. M. Glovsky, R. C. Flagan, and M. O. Andreae (2003), Composition and
778 diurnal variability of the natural Amazonian aerosol, *J. Geophys. Res.-Atmos.*, *108*(D24).
779
780 Heintzenberg, J. (2009), The SAMUM-1 experiment over Southern Morocco: overview
781 and introduction, *Tellus Ser. B-Chem. Phys. Meteorol.*, *61*(1), 2-11.
782
783 Hill, S. C., A. C. Hill, and P. W. Barber (1984), Light-scattering by size shape
784 distributions of soil particles and spheroids, *Applied Optics*, *23*(7), 1025-1031.
785
786 Hu, Y., D. Winker, M. Vaughan, B. Lin, A. Omar, C. Trepte, D. Flittner, P. Yang, S. L.
787 Nasiri, B. Baum, W. Sun, Z. Liu, Z. Wang, S. Young, K. Stamnes, J. Huang, R. Kuehn,
788 and R. Holz (2009), CALIPSO/CALIOP Cloud Phase Discrimination Algorithm, *J.*
789 *Atmos. Oceanic Technol.*, ***26***, 2293-2309.
790
791 Iman, R. L., and W. J. Conover (1980), Small sample sensitivity analysis techniques for
792 computer-models, with an application to risk assessment, *Communications in Statistics*
793 *Part a-Theory and Methods*, *9*(17), 1749-1842.
794
795 Ismail, S., R. A. Ferrare, E. V. Browell, S. A. Kooi, J. P. Dunion, G. Heymsfield, A. Notari, C.
796 F. Butler, S. Burton, M. Fenn, T. N. Krishnamurti, M. K. Biswas, G. Chen, and B. Anderson

(2010), LASE measurements of water vapor, aerosol, and cloud distributions in Saharan air layers and Tropical disturbances
*J. Atmos. Sci.*, *In Press*.

Israelevich, P. L., E. Ganor, Z. Levin, and J. H. Joseph (2003), Annual variations of physical properties of desert dust over Israel, *J. Geophys. Res.*, *108*.

Kalashnikova, O. V., and I. N. Sokolik (2002), Importance of shapes and compositions of wind-blown dust particles for remote sensing at solar wavelengths, *Geophys. Res. Letts.*, *29*(10), 38 31-34.

Kalashnikova, O. V., and I. N. Sokolik (2004), Modeling the radiative properties of nonspherical soil-derived mineral aerosols, *J. Quant. Spectroscopy & Radiative Transfer*, *87*(2), 137-166.

Kandler, K., L. Schutz, C. Deutscher, M. Ebert, H. Hofmann, S. Jackel, R. Jaenicke, P. Knippertz, K. Lieke, A. Massling, A. Petzold, A. Schladitz, B. Weinzierl, A. Wiedensohler, S. Zorn, and S. Weinbruch (2009), Size distribution, mass concentration, chemical and mineralogical composition and derived optical parameters of the boundary layer aerosol at Tinfou, Morocco, during SAMUM 2006, *Tellus Ser. B-Chem. Phys. Meteorol.*, *61*(1), 32-50.

Kaufman, Y. J., I. Koren, L. A. Remer, D. Tanre, P. Ginoux, and S. Fan (2005), Dust transport and deposition observed from the Terra-Moderate Resolution Imaging Spectroradiometer ( MODIS) spacecraft over the Atlantic ocean, *J. Geophys. Res.-Atmos.*, *110*(D10).

Liu, Z., A. Omar, M. Vaughan, J. Hair, C. Kittaka, Y. X. Hu, K. Powell, C. Trepte, D. Winker, C. Hostetler, R. Ferrare, and R. Pierce (2008), CALIPSO lidar observations of the optical properties of Saharan dust: A case study of long-range transport, *J. Geophys. Res.*, *113*(D7).

Liu, Z. Y., M. Vaughan, D. Winker, C. Kittaka, B. Getzewich, R. Kuehn, A. Omar, K. Powell, C. Trepte, and C. Hostetler (2009), The CALIPSO Lidar Cloud and Aerosol Discrimination: Version 2 Algorithm and Initial Assessment of Performance, *J. Atmos. Oceanic Technol.*, *26*(7), 1198-1213.

Maring, H., D. L. Savoie, M. A. Izaguirre, L. Custals, and J. S. Reid (2003), Mineral dust aerosol size distribution change during atmospheric transport, *J. Geophys. Res.*, *108*(D19).

Mie, G. (1908), Beigrade zur optik trüber medien, speziell kolloidaler metallösungen, *Ann. Physik*, *25*(4), 337-445.

841 Mischenko, M. I., A. A. Lacis, B. E. Carlson, and L. D. Travis (1995), Nonsphericity of
842 dust-like tropospheric aerosols: implications for aerosol remote sensing and climate
843 modeling, *Geophys. Res. Letts.*, *22*(9), 1077-1080.
844
845 Mishchenko, M. I. (1991), Light-scattering by randomly oriented axially symmetrical
846 particles, *J. Opt. Soc. Am. A*, *8*(6), 871-882.
847
848 Mishchenko, M. I. (1993), Light-scattering by size shape distributions of randomly
849 oriented axially-symmetrical particles of a size comparable to a wavelength, *Applied*
850 *Optics*, *32*(24), 4652-4666.
851
852 Mishchenko, M. I., and L. D. Travis (1994), T-matrix computations of light-scattering by
853 large spheroidal particle, *Optics Comm.*, *109*(1-2), 16-21.
854
855 Mishchenko, M. I., L. D. Travis, and A. Macke (1996a), Scattering of light by
856 polydisperse, randomly oriented, finite circular cylinders, *Applied Optics*, *35*(24), 4927-
857 4940.
858
859 Mishchenko, M. I., L. D. Travis, and D. W. Mackowski (1996b), T-matrix computations
860 of light scattering by nonspherical particles: A review, *J. Quant. Spectros. Rad. Trans.*,
861 *55*(5), 535-575.
862
863 Mishchenko, M. I., and L. D. Travis (1998), Capabilities and limitations of a current
864 FORTRAN implementation of the T-matrix method for randomly oriented, rotationally
865 symmetric scatterers.
866
867 Morgan, M. G., and M. Henrion (1990), *Uncertainty: A Guide to dealing with*
868 *uncertainty in quantitative risk and policy analysis*, 2 ed., 332 pp., Cambridge University
869 Press, Cambridge.
870
871 Muller, D., A. Ansmann, I. Mattis, M. Tesche, U. Wandinger, D. Althausen, and G.
872 Pisani (2007), Aerosol-type-dependent lidar ratios observed with Raman lidar, *J.*
873 *Geophys. Res.*, *112*(D16).
874
875 Müller, D., F. Wagner, D. Althausen, U. Wandinger, and A. Ansmann (2000), Physical
876 properties of the Indian aerosol plume derived from six-wavelength lidar observations on
877 25 March 1999 of the Indian Ocean Experiment, *Geophys. Res. Letts.*, *27*(9), 1403-1406.
878
879 Murayama, T., S. J. Masonis, J. Redemann, T. L. Anderson, B. Schmid, J. M. Livingston,
880 P. B. Russell, B. Huebert, S. G. Howell, C. S. McNaughton, A. Clarke, M. Abo, A.
881 Shimizu, N. Sugimoto, M. Yabuki, H. Kuze, S. Fukagawa, K. Maxwell-Meier, R. J.
882 Weber, D. A. Orsini, B. Blomquist, A. Bandy, and D. Thornton (2003), An
883 intercomparison of lidar-derived aerosol optical properties with airborne measurements
884 near Tokyo during ACE-Asia, *J. Geophys. Res.*, *108*(D23).
885

886 Nakajima, T., M. Tanaka, M. Yamano, M. Shiobara, K. Arao, and Y. Nakanishi (1989),
887 Aerosol optical characteristics in the yellow sand events observed in may, 1982 at
888 Nagasaki .2. Models, *J. Meteor. Soc. Japan*, *67*(2), 279-291.
889
890 Okada, K., A. Kobayashi, Y. Iwasaka, H. Naruse, T. Tanaka, and O. Nemoto (1987),
891 Features of individual asian dust-storm particles collected at Nagoya, Japan, *J. Meteor.*
892 *Soc. Japan*, *65*(3), 515-521.
893
894 Okin, G. S., N. Mahowald, O. A. Chadwick, and P. Artaxo (2004), Impact of desert dust
895 on the biogeochemistry of phosphorus in terrestrial ecosystems, *Global Biogeochemical*
896 *Cycles*, *18*(2).
897
898 Omar, A., D. Winker, C. Kittaka, M. Vaughan, Z. Liu, Y. Hu, C. Trepte, R. Rogers, R.
899 Ferrare, K. P. Lee, R. Kuehn, and C. Hostetler (2009), The CALIPSO automated aerosol
900 classification and lidar ratio selection algorithm, *J. Atmos. Oceanic Technol.*, *26*(10),
901 1994-2014.
902
903 Omar, A. H., S. Biegalski, S. M. Larson, and S. Landsberger (1999), Particulate
904 contributions to light extinction and local forcing at a rural Illinois site, *Atmospheric*
905 *Environment*, *33*(17), 2637-2646.
906
907 Perry, R. J., A. J. Hunt, and D. R. Huffman (1978), Experimental determinations of
908 Mueller scattering matrices for nonspherical particles
909 *Applied Optics*, *17*(17), 2700-2710.
910
911 Petzold, A., K. Rasp, B. Weinzierl, M. Esselborn, T. Hamburger, A. Dornbrack, K.
912 Kandler, L. Schutz, P. Knippertz, M. Fiebig, and A. Virkkula (2009), Saharan dust
913 absorption and refractive index from aircraft-based observations during SAMUM 2006,
914 *Tellus Ser. B-Chem. Phys. Meteorol.*, *61*(1), 118-130.
915
916 Platt, C. M. R. (1973), Lidar and Radiometric Observations of Cirrus Clouds, *J. Atmos.*
917 *Sci.*, *30*, 1191-1204.
918
919 Prospero, J. M., and T. N. Carlson (1971), Saharan dust in atmosphere of northern
920 equatorial Atlantic ocean - a major constituent of marine aerosol
921 *Bulletin of the American Meteorological Society*, *52*(11), 1138-&.
922
923 Prospero, J. M., and T. N. Carlson (1972), Vertical and areal distribution of Saharan dust
924 over western equatorial North-Atlantic Ocean
925 *J. Geophys. Res.*, *77*(27), 5255-5265.
926
927 Rodhe, H. (2009), Special issue: Results of the Saharan Mineral Dust Experiment
928 (SAMUM-1) 2006 Preface, *Tellus Ser. B-Chem. Phys. Meteorol.*, *61*(1), 1-1.
929

930 Sasano, Y., and E. V. Browell (1989), Light scattering characteristics of various aerosol
931 types derived from multiple wavelength lidar observations, *Applied Optics*, *28*, 1670-
932 1679.
933
934 Savoie, D., and J. M. Prospero (1976), Saharan aerosol transport across Atlantic ocean -
935 characteristics of input and output, *Bull Am. Meteorol. Soc.*, *57*(1), 145-145.
936
937 Schladitz, A., T. Muller, N. Kaaden, A. Massling, K. Kandler, M. Ebert, S. Weinbruch,
938 C. Deutscher, and A. Wiedensohler (2009), In situ measurements of optical properties at
939 Tinfou (Morocco) during the Saharan Mineral Dust Experiment SAMUM 2006, *Tellus*
940 *Ser. B-Chem. Phys. Meteorol.*, *61*(1), 64-78.
941
942 Sokolik, I. N., and O. B. Toon (1996), Direct radiative forcing by anthropogenic airborne
943 mineral aerosols, *Nature*, *381*(6584), 681-683.
944
945 Tesche, M., A. Ansmann, D. Muller, D. Althausen, I. Mattis, B. Heese, V. Freudenthaler,
946 M. Wiegner, M. Esselborn, G. Pisani, and P. Knippertz (2009), Vertical profiling of
947 Saharan dust with Raman lidars and airborne HSRL in southern Morocco during
948 SAMUM, *Tellus B*, *61*(1), 144-164.
949
950 Vaughan, M. A., Z. Liu, and A. H. Omar (2004), Multi-wavelength analysis of a lofted
951 aerosol layer measured by LITE, paper presented at 22nd International Laser Radar
952 Conference, European Space Agency, Matera, Italy, 12-16 July, 2004.
953
954 Vaughan, M. A., K. A. Powell, R. E. Kuehn, S. A. Young, D. M. Winker, C. A.
955 Hostetler, W. H. Hunt, Z. Y. Liu, M. J. McGill, and B. J. Getzewich (2009), Fully
956 Automated Detection of Cloud and Aerosol Layers in the CALIPSO Lidar
957 Measurements, *J. Atmos. Oceanic Technol.*, *26*(10), 2034-2050.
958
959 Virkkula, A., N. C. Ahlquist, D. S. Covert, W. P. Arnott, P. J. Sheridan, P. K. Quinn, and
960 D. J. Coffman (2005), Modification, calibration and a field test of an instrument for
961 measuring light absorption by particles, *Aerosol Sci. Technol.*, *39*(1), 68-83.
962
963 Volz, F. E. (1973), Infrared Optical Constants of Ammonium Sulfate, Sahara Dust,
964 Volcanic Pumice, and Flyash, *Appl. Opt.*, *12*(3), 564-568.
965
966 Voss, K. J., E. J. Welton, P. K. Quinn, J. Johnson, A. M. Thompson, and H. R. Gordon
967 (2001), Lidar measurements during Aerosols99, *J. Geophys. Res.*, *106*(D18), 20821-
968 20831.
969
970 Waterman, P. C. (1971), Symmetry, unitarity, and geometry in electromagnetic
971 scattering, *Physical Review D*, *3*(4), 825-&.
972
973 Winker, D., M. Vaughan, A. Omar, Y. Hu, K. Powell, Z. Liu, W. Hunt, and S. A. Young
974 (2009), Overview of the CALIPSO mission and CALIOP data processing algorithms *J.*
975 *Atmos. Ocean. Tech.*, *26*, 2310-2323.

Winker, D. M., W. H. Hunt, and M. J. McGill (2007), Initial performance assessment of CALIOP, *Geophys. Res. Letts.*, *34*(19).

Wong, S., and A. E. Dessler (2005), Suppression of deep convection over the tropical North Atlantic by the Saharan Air Layer, *Geophysical Research Letters*, *32*(9).

Young, S. A. (1995), Analysis of lidar backscatter profiles in optically thin clouds, *Applied Optics*, *34*(30), 7019-7031.

Figure 1. (a) A Two-dimensional probability plot of NAMMA in situ size distributions measured in a dust layer over a 22 minute period (~260 size distributions) during Flight 4 on August 19, 2006. The mean measured size distribution is denoted by the yellow line, and (b) the best approximate bimodal log-normal particle size distribution (blue squares) with fine (coarse) mean radius of 0.0648 (0.5627) μm and a fine (coarse) geometric standard deviation of 1.696 (1.572) fitted to the average measured size distribution (red squares).

995

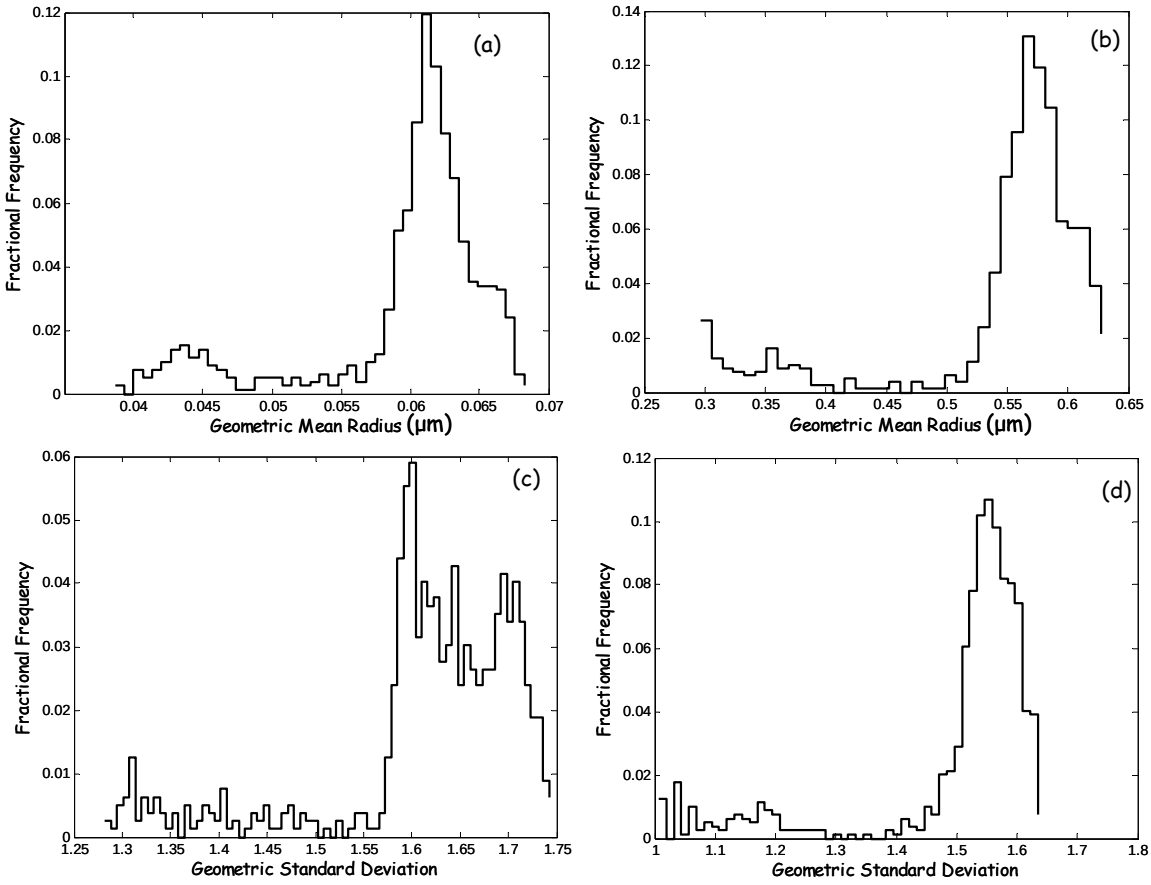


996

997 Figure 2. The distributions of the fine (a) and coarse (b) geometric mean radii and the
998 fine (c) and coarse (d) geometric standard deviations for a dense elevated dust layer
999 measured during a flight on August 25, 2006.
1000

1001

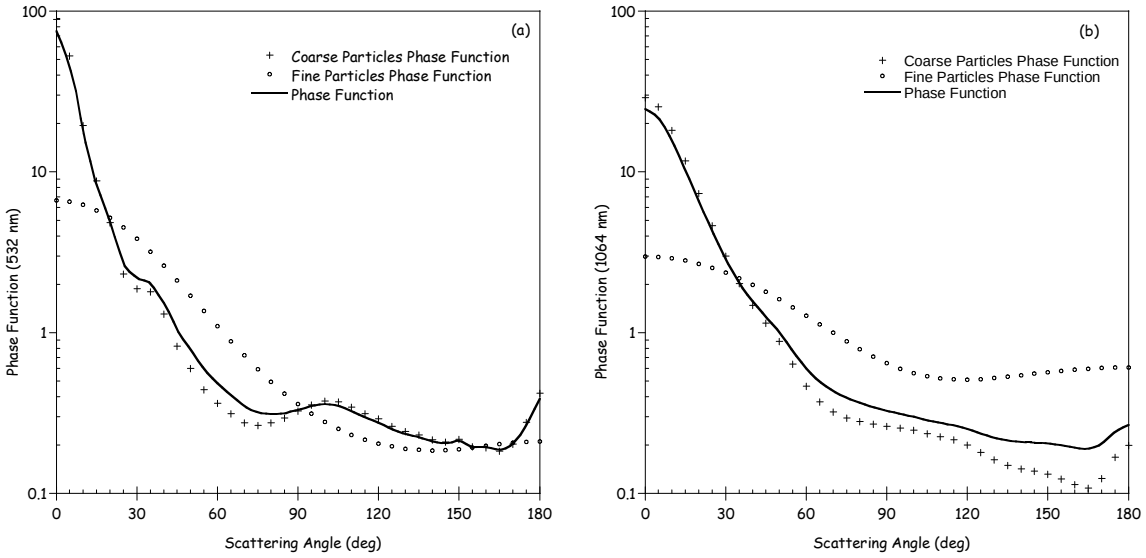


1002

1003 Figure 3. The (a) 532-nm and (b) 1064 nm Saharan dust phase functions calculated from
1004 the size distributions measured aboard NASA DC-8 during Flight 4 on August 19, 2006.
1005

1006

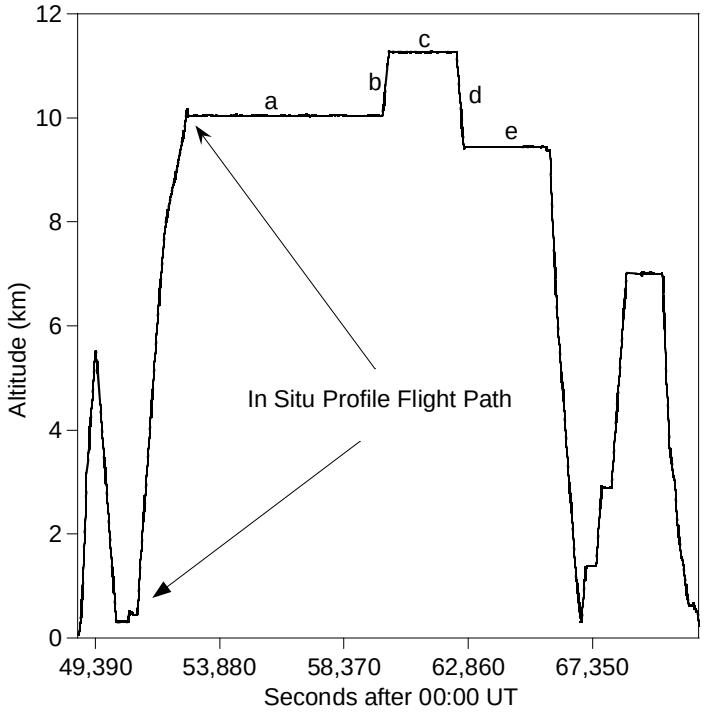


1007

1008 Figure 4. The DC-8 altitudinal flight path showing the segment during which the in situ
1009 measurements were made. The direct CALIPSO underflights are the five segments (a, b,
1010 c, d, and e) at the highest altitudes. The time is in seconds after midnight UTC.
1011

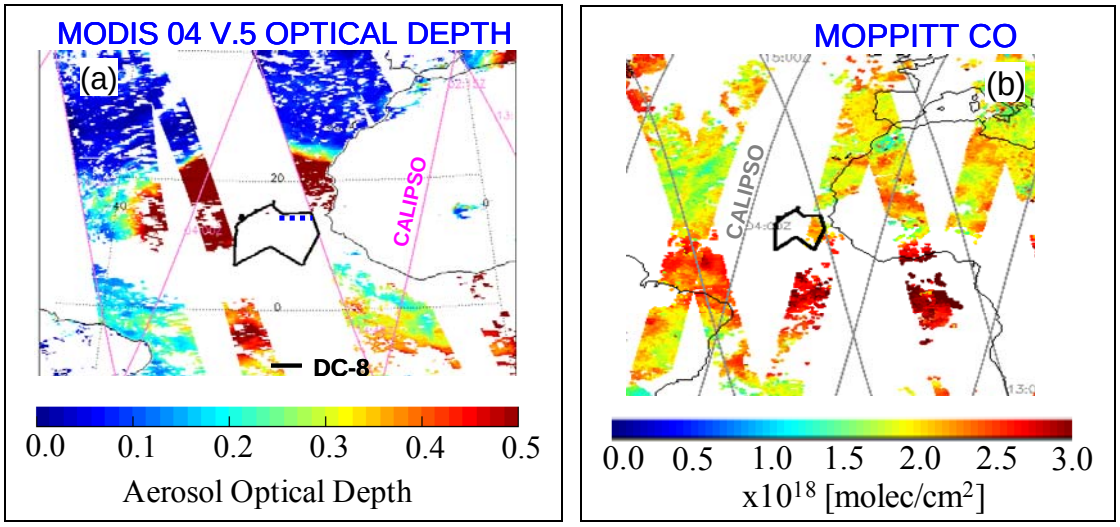


Figure 5. CALIPSO flight tracks superimposed on (a) the MODIS optical depth and (b) the MOPPITT CO concentrations. The DC-8 flight track for August 19, 2006 is shown by the black lines in the middle of both figures. The blue dots in (a) denote the portion of the DC-8 flight segment during which the in-situ measurements were taken. Daytime CALIPSO tracks run from the southeast to the northwest while the nighttime tracks run from northeast to the southwest.

1021

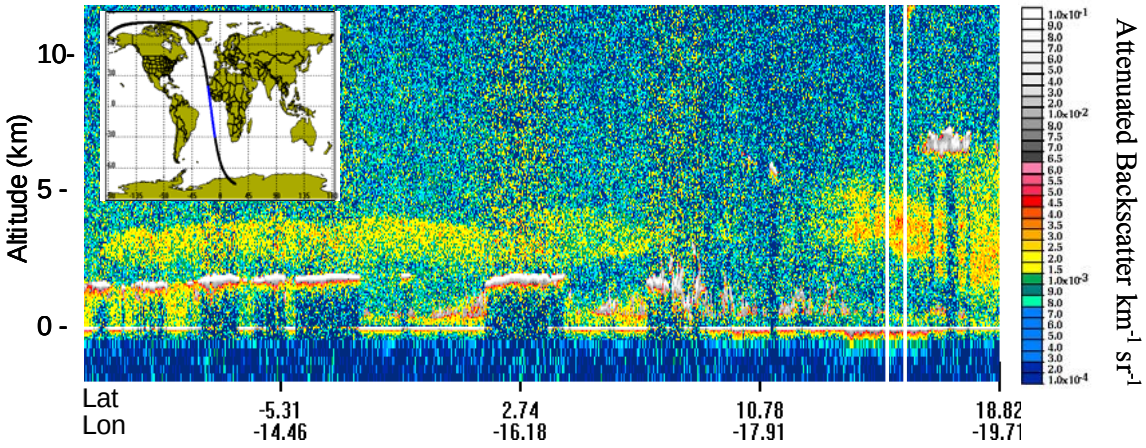


1022

1023 Figure 6. Browse image of the CALIPSO flight track on August 19, 2006 shown in blue
1024 in the inset map and the location of the near coincidence of the CALIPSO flight track and
1025 the DC-8 flight 4 during NAMMA is denoted by the two white lines near 15N, 19W. In
1026 the image, colors above the surface are coded as follows: blue indicates clear sky, white
1027 indicates clouds, and warm colors (green, yellow, orange, and red) indicate aerosols. The
1028 white parallel lines bound the CALIPSO profiles closest to the in-situ measurements.
1029

1030

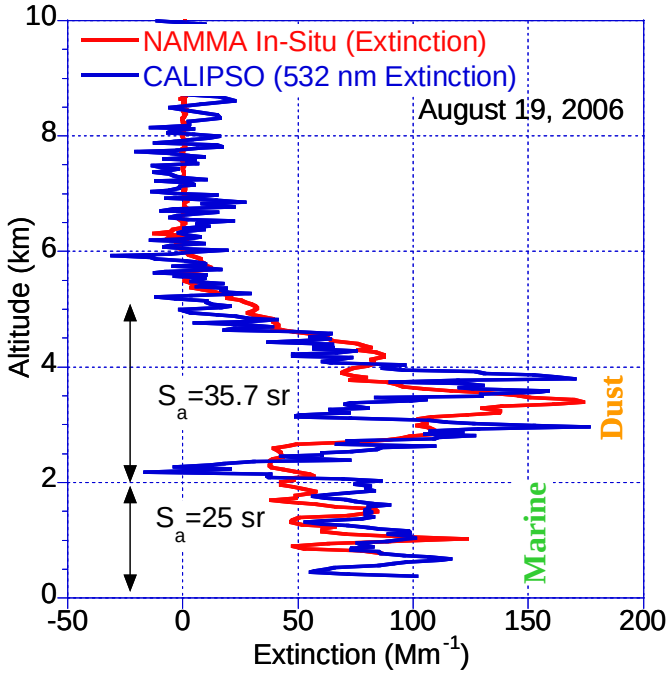


1031

1032 Figure 7. A comparison of the profiles of the in situ extinction coefficient derived during
1033 the DC-8 ascending segment as shown in Figure 4 and the extinction coefficient retrieved
1034 from the CALIPSO measurement averaged over the region indicated by the two white
1035 lines in Figure 6. The $S_a$ ratios were determined using the in situ extinction as an
1036 additional constraint.
1037

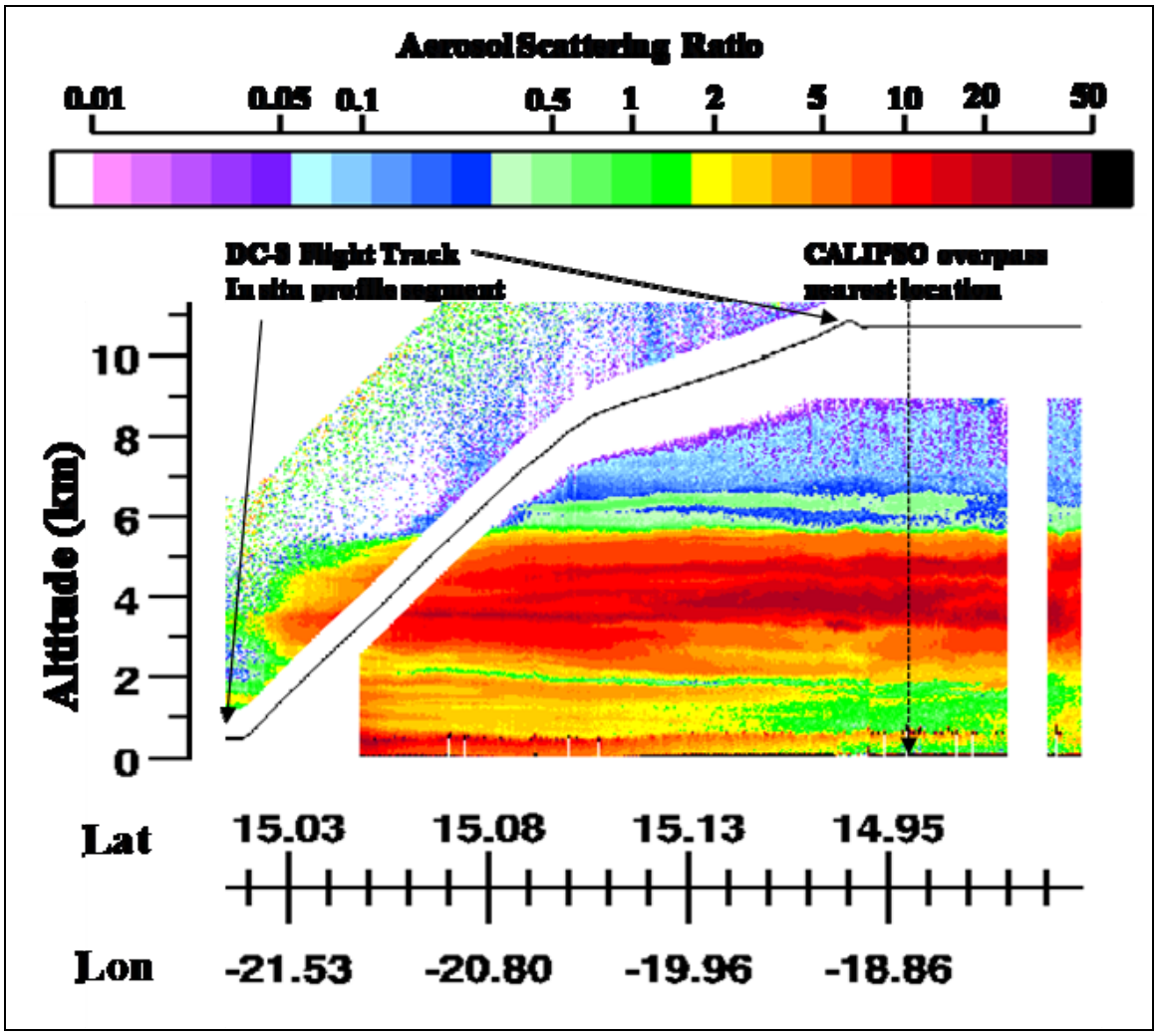


1038

1039 Figure 8. Aerosol scattering ratio ($\beta_a/\beta_m$ at 815 nm) image measured by the Lidar
1040 Atmospheric Sensing Experiment (LASE) aboard DC-8 during the ascending segment
1041 passing through a Sahara Air Layer (SAL) and the underflight of CALIPSO as shown in
1042 Figure 4. The DC-8 point of nearest approach to the CALIPSO flight track is near 15°N-
1043 19°W.
1044

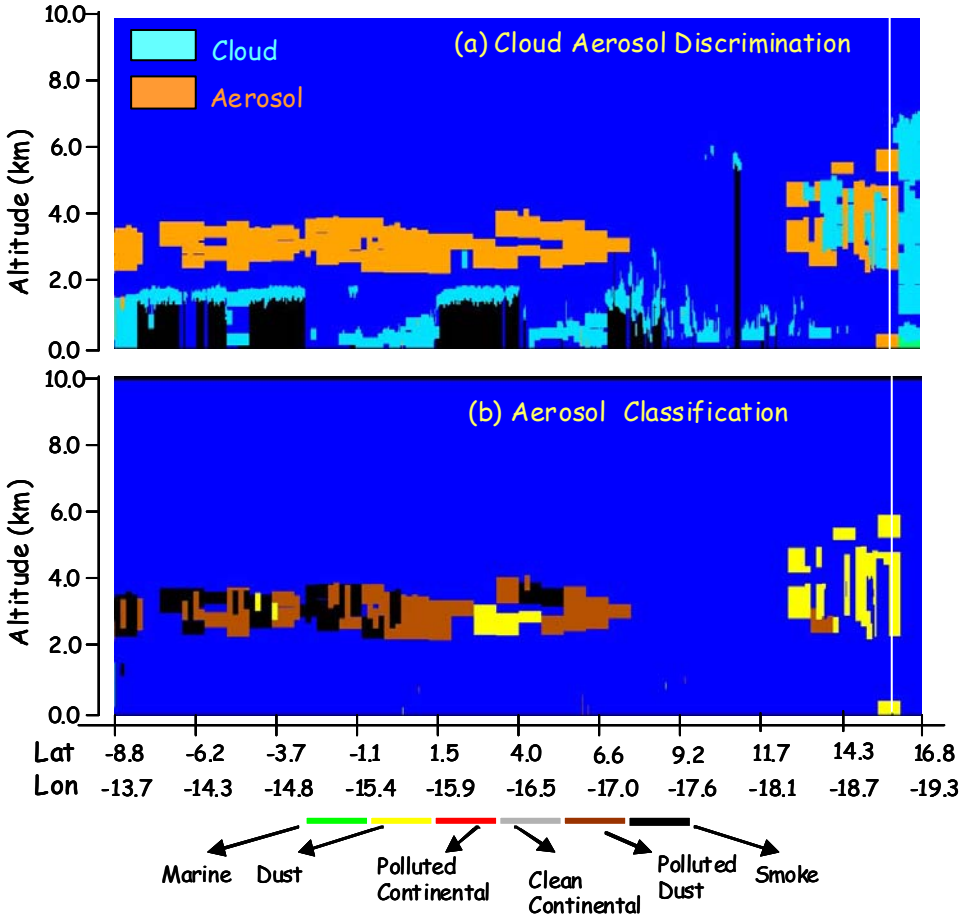


1045

1046 Figure 9. Products of the CALIPSO (a) cloud-aerosol discrimination and (b) aerosol
1047 classification schemes for the data in the browse image shown in Figure 6. The cloud
1048 aerosol discrimination shows the extensive aerosol layer at 3 km and the aerosol
1049 classification image shows that this aerosol is a Saharan dust layer to the north and a
1050 polluted dust and smoke layer to the south.
1051

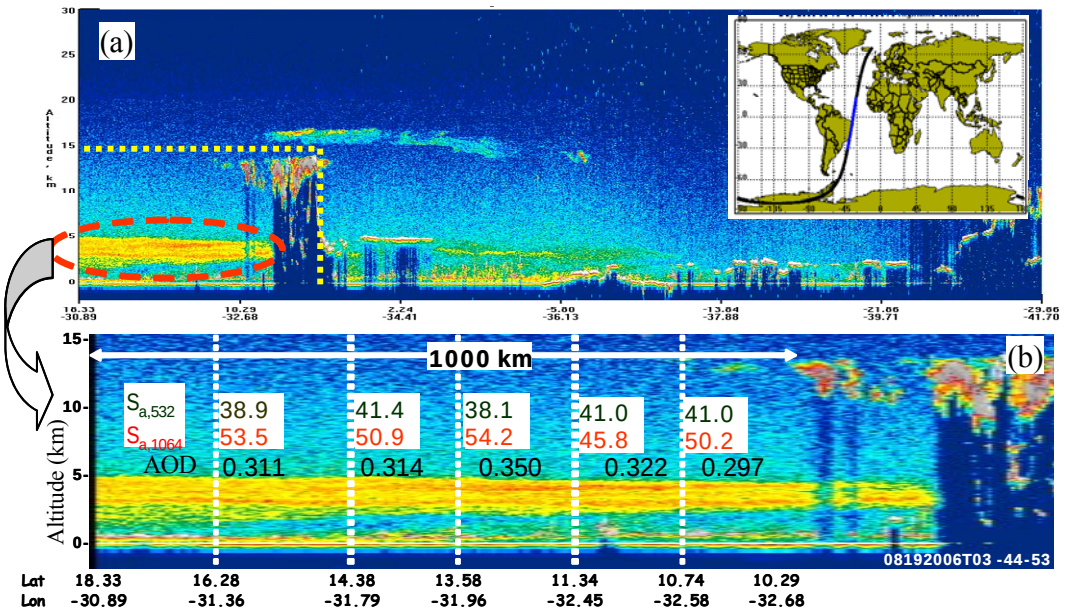


Figure 10. (a) Browse image of the orbit segment denoted by the blue track in the inset map and (b) an expansion of the dust layer region of the plot marked by yellow dots in (a). In both cases the color code is as in Figure 6. The red dashed oval shows the elevated (layer top ~ 5km) dust layer. Aerosol optical depths at 532 nm for all five segments are shown on the figure and are near 0.3.

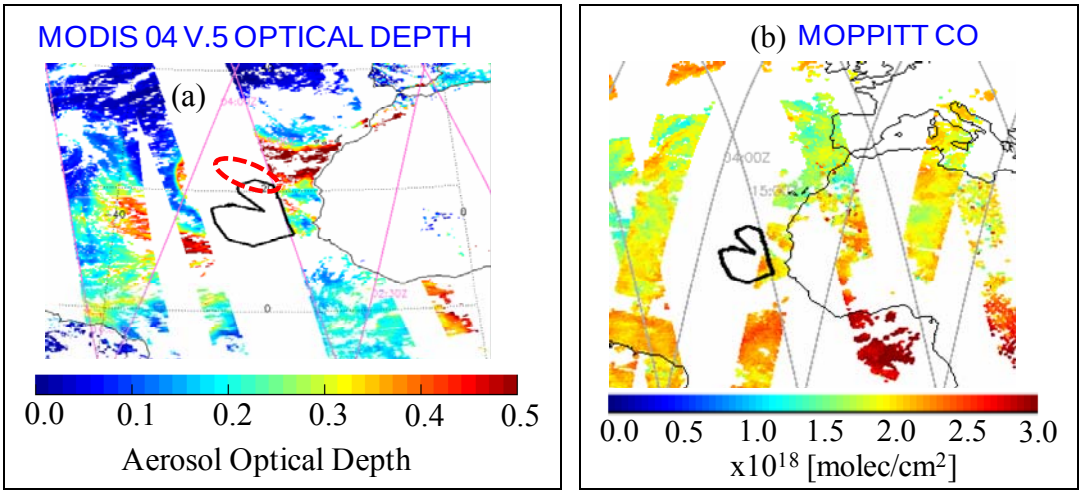


Figure 11. CALIPSO flight tracks superimposed on the (a) MODIS optical depth and the (b) MOPPITT CO concentrations. The CALIPSO flight tracks are colored cyan and grey in the MODIS and MOPPITT images, respectively. The DC-8 flight track for August 26, 2006 is shown by the heart shaped drawing in the middle of both figures. The CALIPSO underflight segment is the portion of the flight track in alignment with the CALIPSO flight track in cyan or grey in (a) or (b), respectively. The DC-8 in situ data for this obtained during the descent flight segment shown by a red dashed tilted oval in (a).

1069

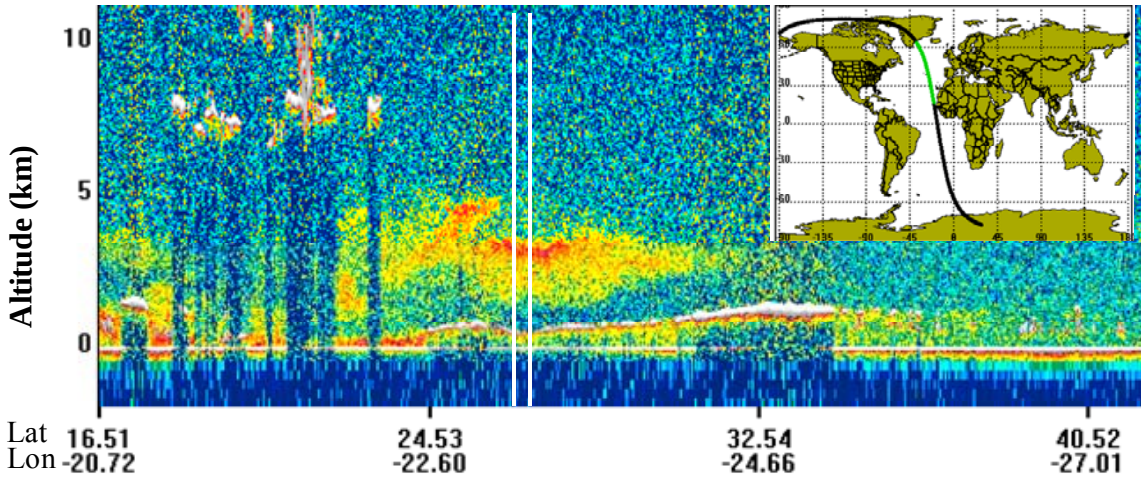


1070

1071 Figure 12. Browse image of the CALIPSO flight track shown in green in the inset map
1072 and the location of the near coincidence (in space) of the CALIPSO flight track and the
1073 DC-8 flight 8 on August 26, 2006. The color code is as in Fig. 6. The white lines denote
1074 the CALIPSO data used for comparison with the DC-8 measurements.
1075

1076

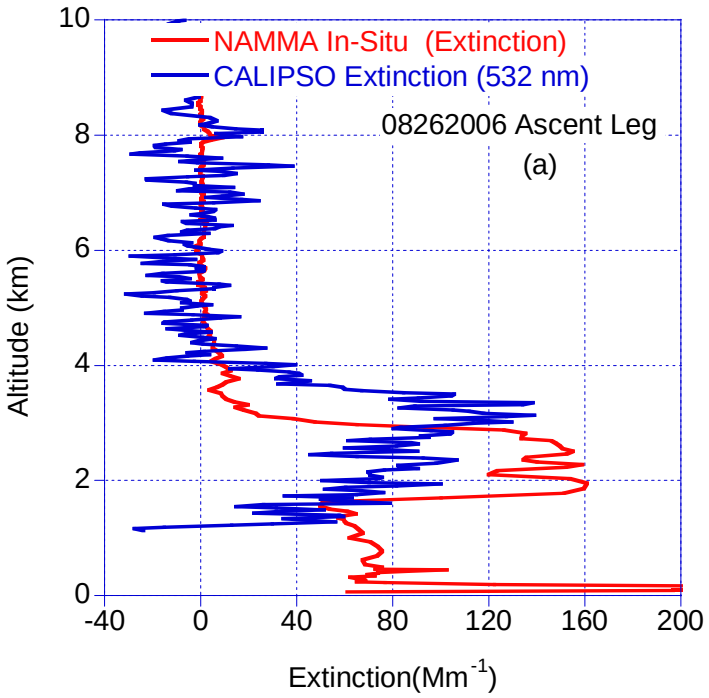


1077

1078 Figure 13. A comparison of the NAMMA in situ extinction profile and the extinction
1079 profile calculated from CALIPSO's attenuated backscatter measurement using 532 nm $S_a$
1080 ratio of 38.2 sr obtained using the transmittance method. The two measurements both
1081 taken on August 26, 2006 are offset by 2 hours and ~1250 km.
1082

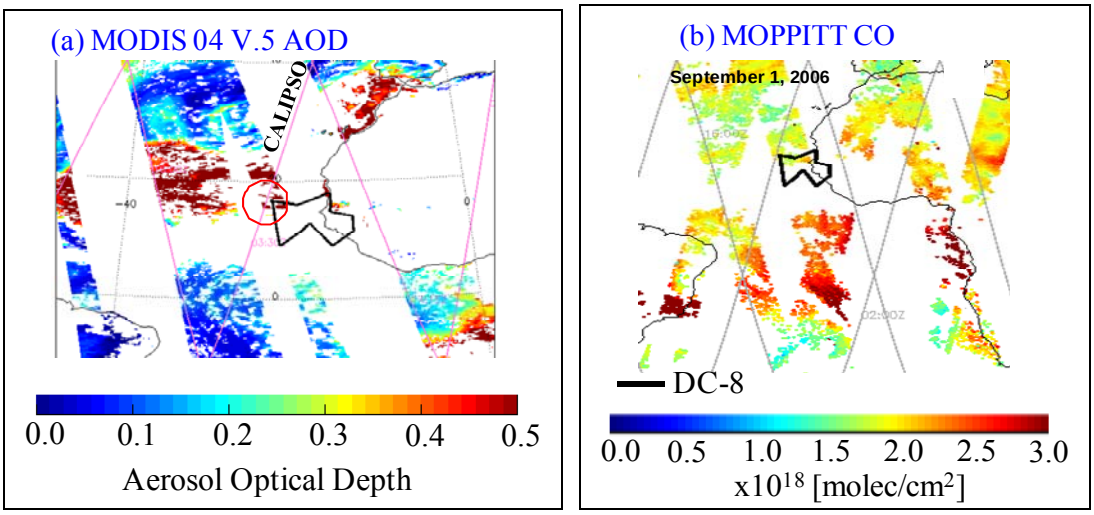


Figure 14. CALIPSO flight tracks superimposed on the (a) MODIS optical depth and the (b) MOPPITT CO concentrations. The CALIPSO flight tracks are colored cyan and grey in the MODIS and MOPPITT images. The DC-8 flight track for September 1, 2006 is shown by the black lines in the middle of both figures.

1090

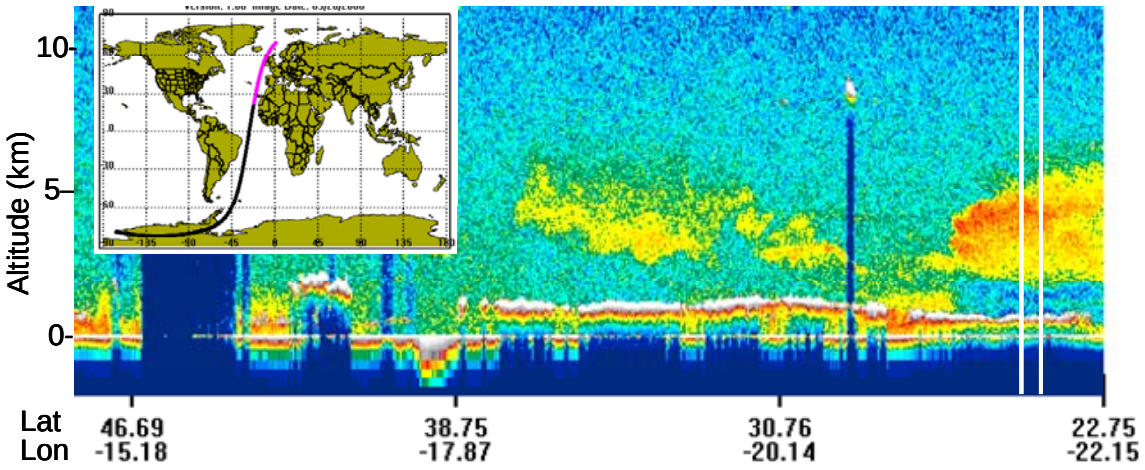


1091

1092 Figure 15. Browse image of the CALIPSO flight track shown in cyan in the inset map
1093 and the location of the near coincidence (in space) of the CALIPSO and the DC-8 flight
1094 tracks on September 1 during NAMMA. The color code is as in Fig. 6. The white lines
1095 subtend the region averaged for the extinction comparison.
1096

1097

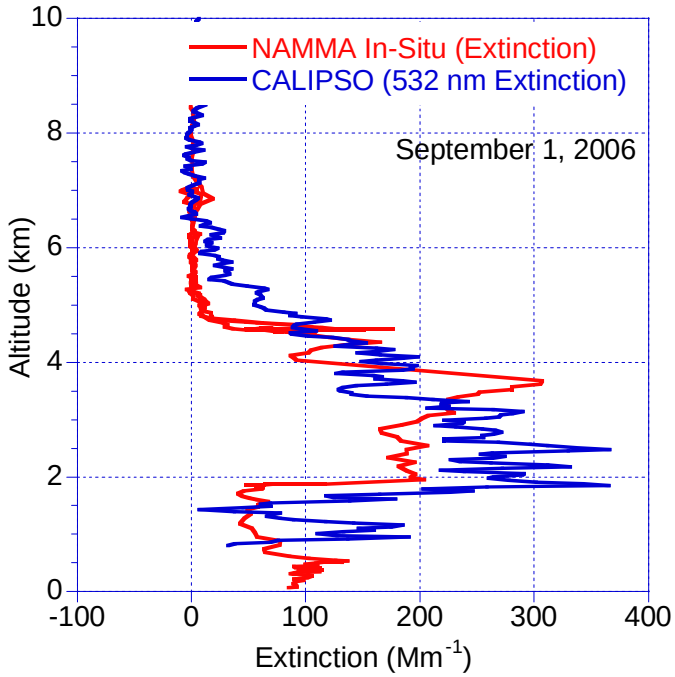


1098

1099 Figure 16. The NAMMA/CALIPSO extinction comparison for Flight 10 on September 1,
1100 2006. Note that the centroid of the layer has shifted upwards by about 1.5 km in between
1101 the CALIPSO measurement and NAMMA sampling. The CALIPSO measurement is ~15
1102 hours earlier and nearly 750 km away.
1103

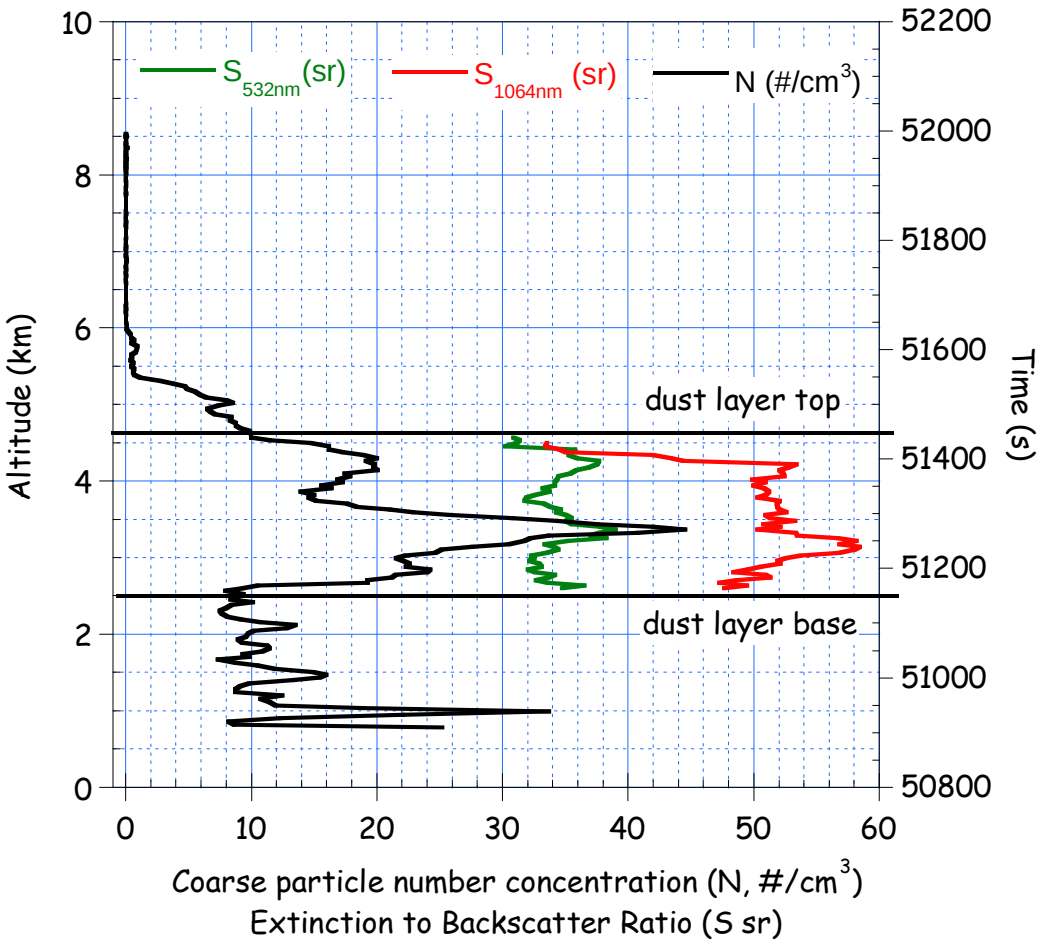


Figure 17. A profile of the 1064 and 532-nm $S_a$ ratios and integrated number distribution of coarse particles (0.583 um – 6.264 um) taken from a 20-minute segment of the APS measurements during Flight 4 on August 19, 2006. The dust base and top are shown by the lines at altitudes of 2.5 km and 4.6 km, respectively. The mean 532-nm and 1064-nm $S_a$ ratios for the layer is 34.3 ± 2.0 sr and 50.2 ± 5.7 sr, respectively.

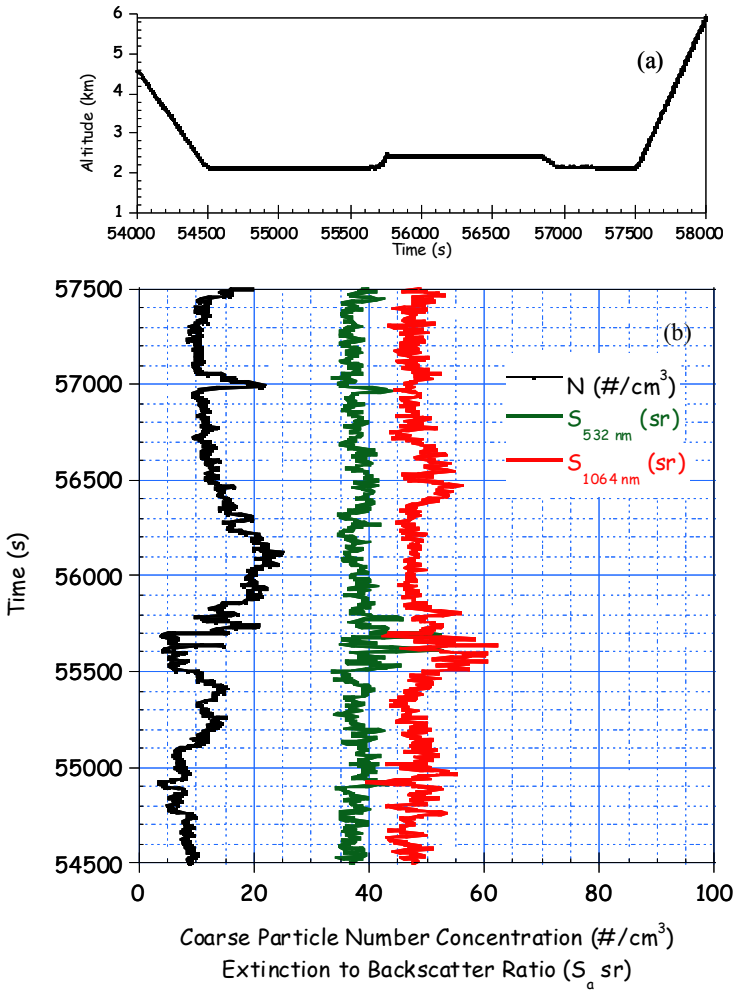


1111

1112 Figure 18. (a) The flight track of the DC-8 on August 25, 2006. The straight and nearly
1113 level portion is through a dust layer at ~2 km. (b) The calculated 532- and 1064-nm $S_a$
1114 ratios and coarse number particle concentration for the straight and level portion of this
1115 flight.
1116

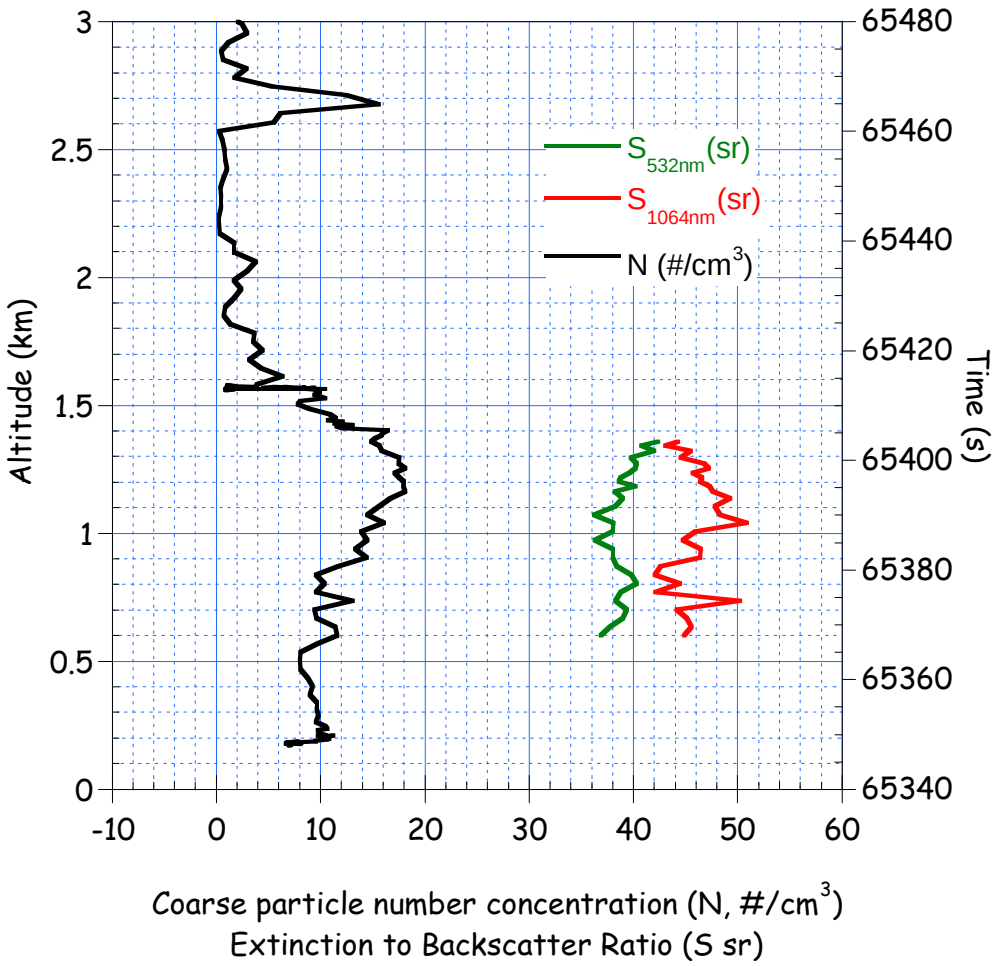


Figure 19. A profile of the 1064- and 532 –nm $S_a$ ratios, and integrated number distribution of coarse particles during Flight 8 on Aug. 26, 2006. The mean 532-nm and 1064-nm $S_a$ ratios for the layer is 39.0 ± 1.5 sr and 45.9 ± 2.2 sr, respectively.

1122

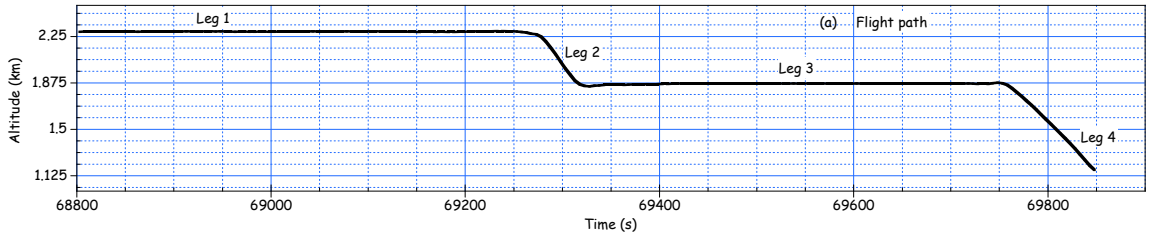


1123

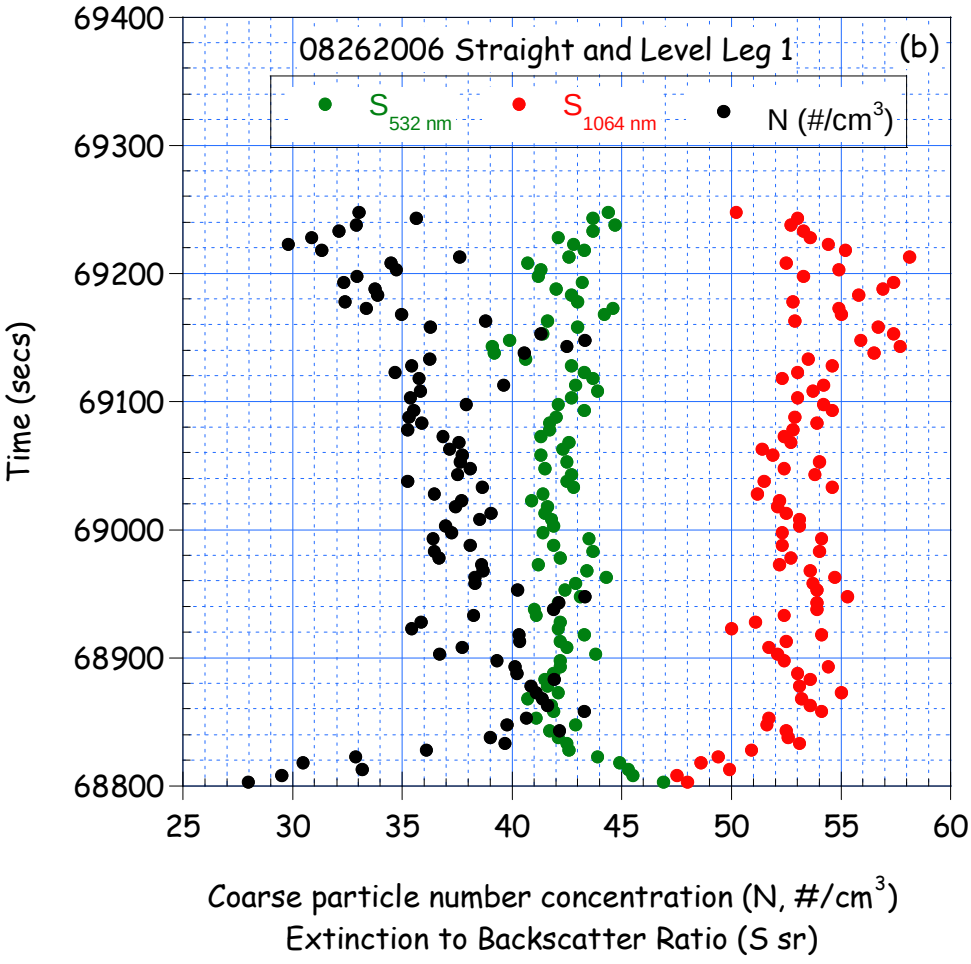


1124

1125

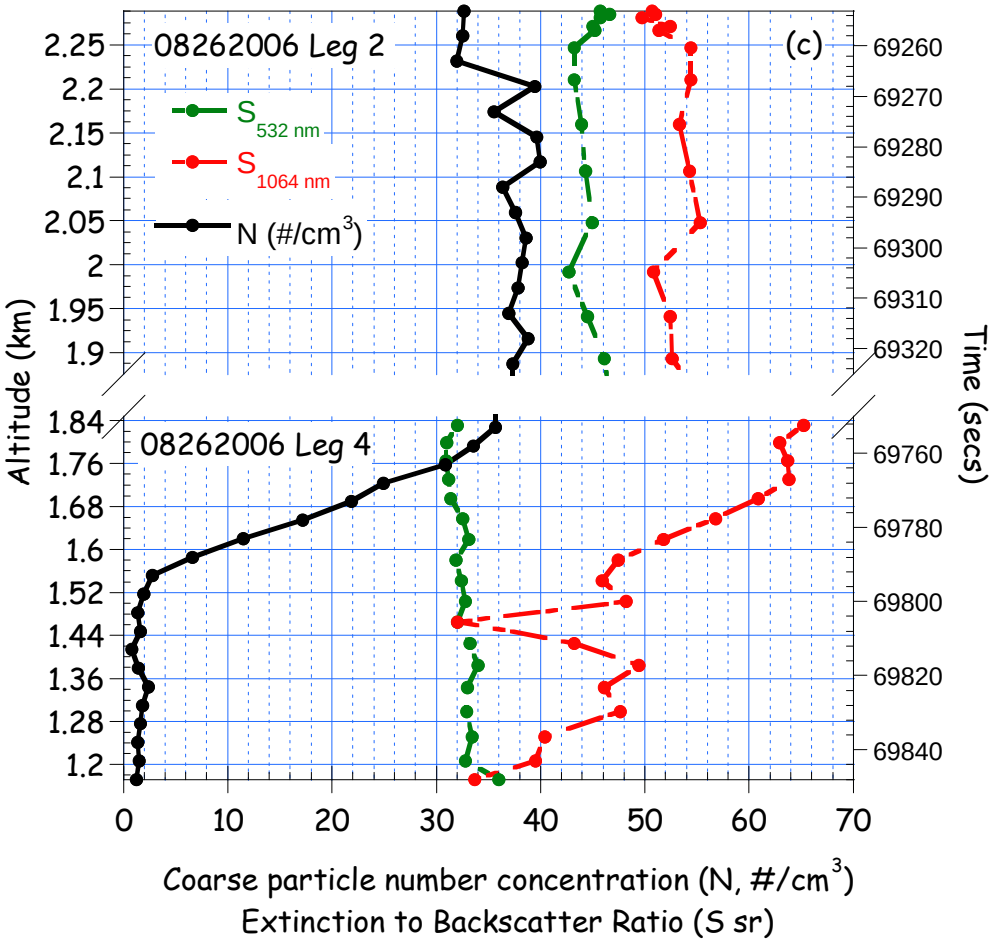
08262006 Leg 2
(c)
S532 nm
S1064 nm
N (#/cm3)
08262006 Leg 4
Altitude (km)
Time (secs)
Coarse particle number concentration (N, #/cm3)
Extinction to Backscatter Ratio (S sr)

1126

1127

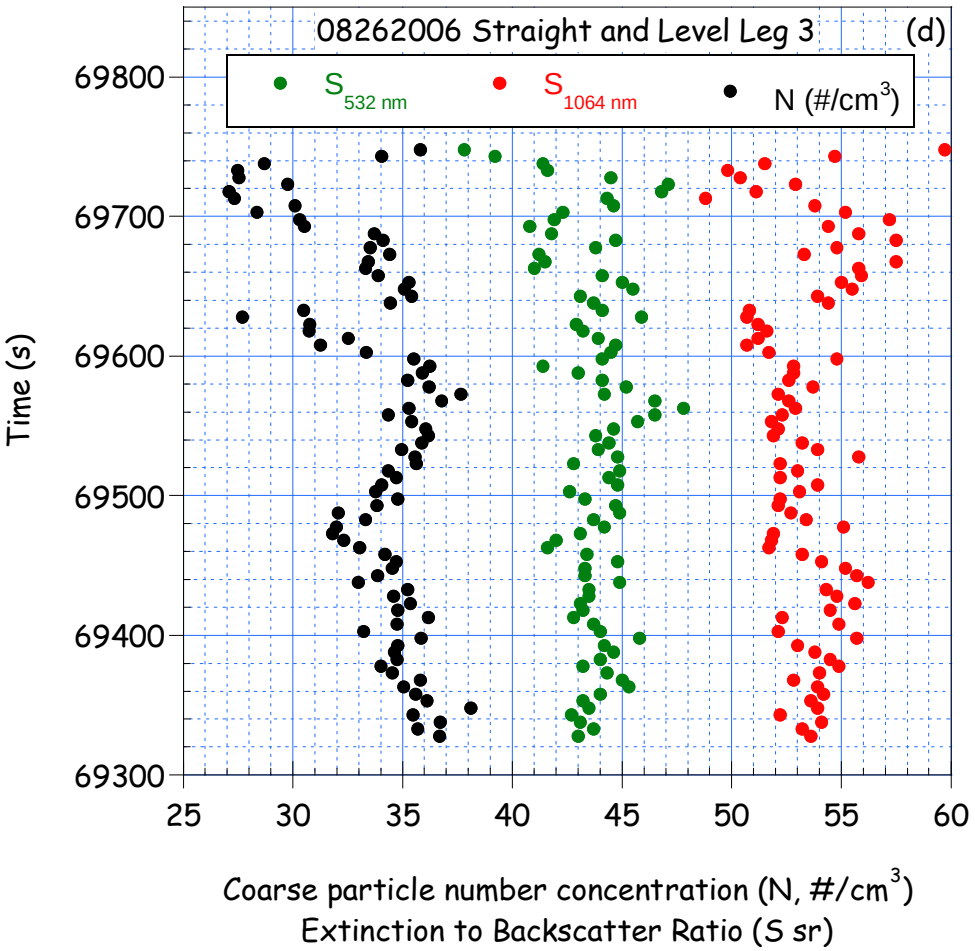


1128

1129 Figure 20 . (a) Flight path and $S_a$ ratios and the particle number concentration for the
1130 return flight on August 26, 2006. The figures are plotted by temporal profiles for the
1131 straight and level legs, and vertical profiles for descent legs. (b) is temporal profile of
1132 straight and level leg 1, (c) vertical profiles of descent legs 2 and 4, and (d) temporal
1133 profile of straight and level leg 3.
1134

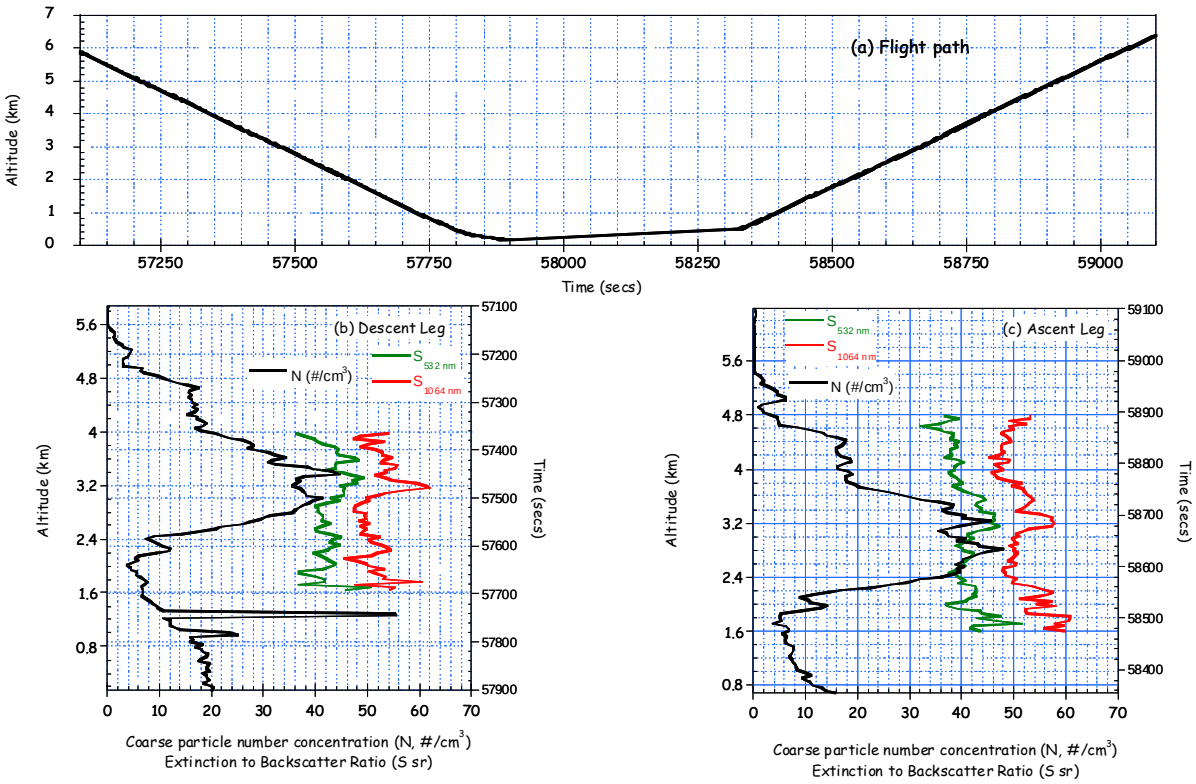


1135

1136 Figure 21.The (a) flight path and $S_a$ ratios and the particle number concentration for the
1137 flight on August 20, 2006 plotted vertical profiles of (b) the descent leg and (c) the ascent
1138 leg.
1139

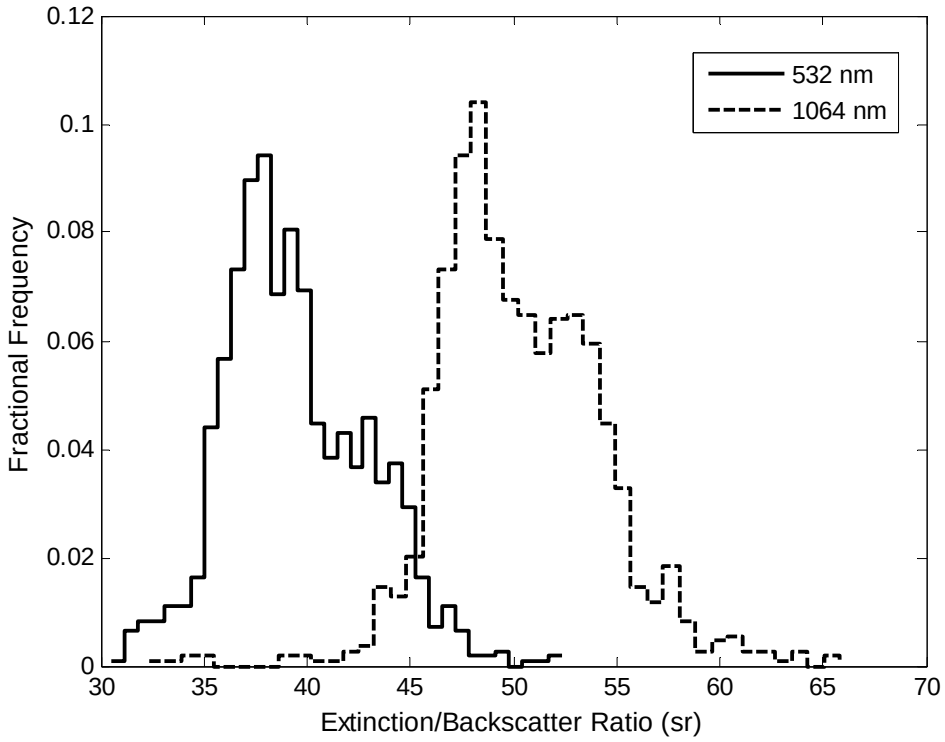


1140

1141 Figure 22. An ensemble of all the $S_a$ ratio estimates (~1100 records) based on the
1142 NAMMA in-situ size distributions of dust layers and T-Matrix calculations. The average
1143 $S_a$ ratios are 39.1 ± 3.5 sr and 50.0 ± 4 sr at 532 nm and 1064 nm, respectively
1144

1145

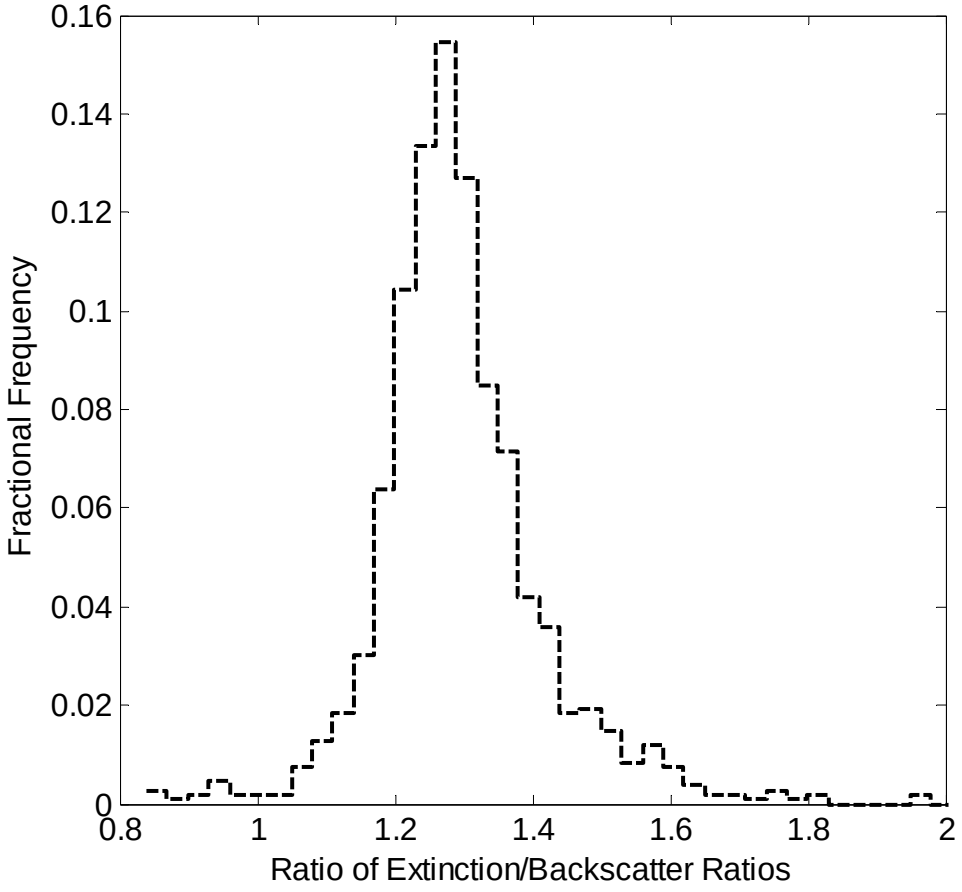


1146

1147 Figure 23. The ratio of the $S_a$ ratios [$S_a$ (1064 nm)/$S_a$ (532 nm)] derived from the size
1148 distribution data used for this study.
1149
1150
1151

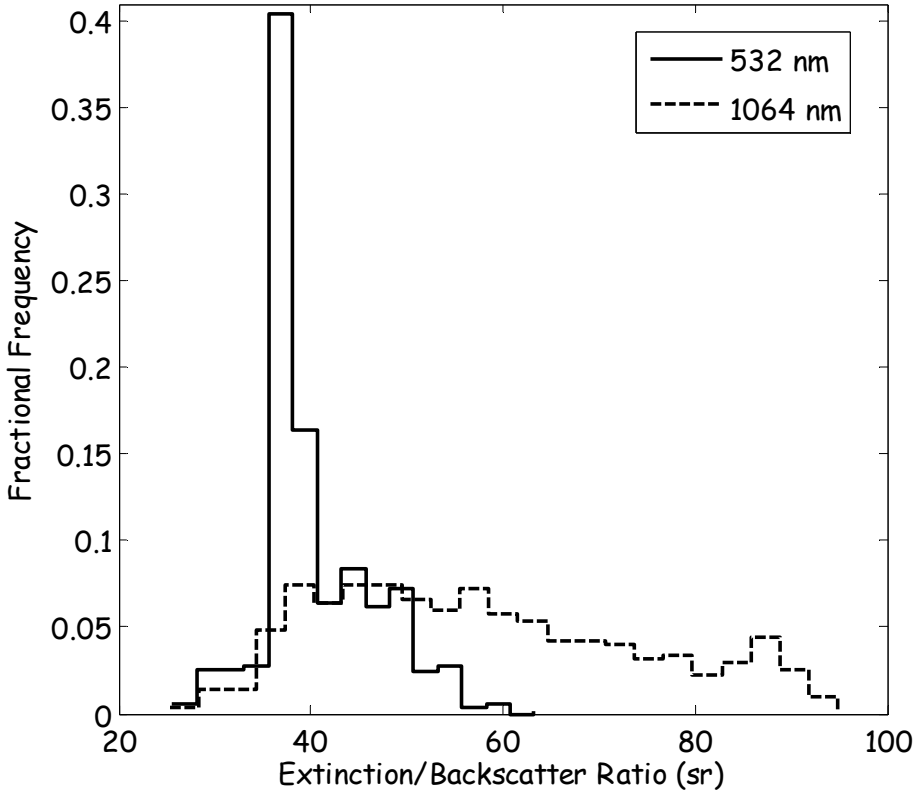


Figure 24. The distribution of the $S_a$ ratio calculated from a Latin Hypercube Sample (LHS) of 500 events bounded by the ranges shown in Table 3. The normal means (± 1 standard deviation) of the 532- and 1064-nm $S_a$ ratios are 39.4 ± 5.9 sr and 56.5 ± 16.5 sr, respectively.

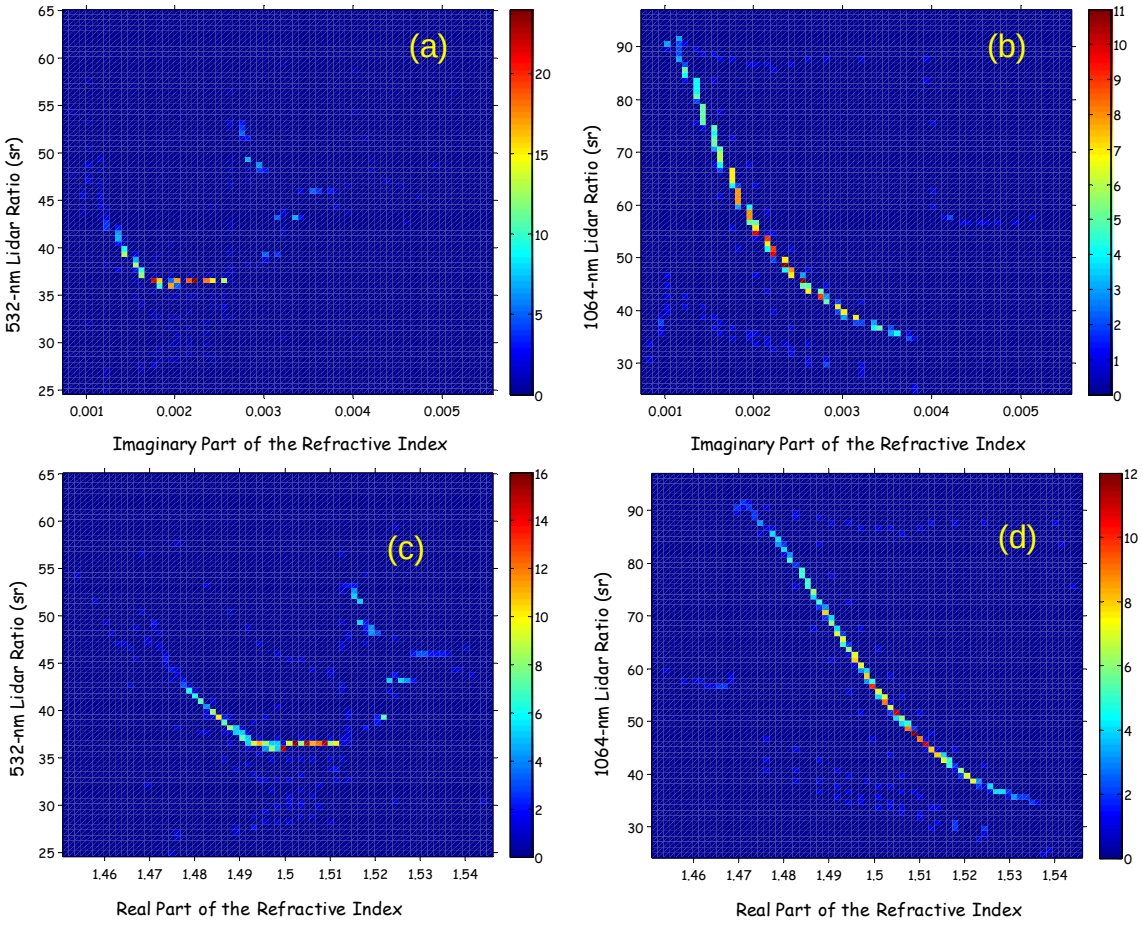


Figure 25. Two-dimensional frequency plots showing the variation of the lidar ratios with real and imaginary parts of the complex refractive indices for 500 randomly generated events discussed in section 6.